³The Effect of Bottom-Generated Tidal Mixing on Tidally Pulsed River Plumes

Preston Spicer, a Kelly L. Cole, a Kimberly Huguenard, a Daniel G. MacDonald, b,c and Michael M. Whitney d

^a Department of Civil and Environmental Engineering, University of Maine, Orono, Maine
^b Department of Estuarine and Ocean Science, School for Marine Science and Technology, University of Massachusetts Dartmouth,

Dartmouth, Massachusetts

(Manuscript received 21 September 2020, in final form 23 February 2021)

ABSTRACT: The mixing of river plumes into the coastal ocean influences the fate of riverborne tracers over the inner shelf, though the relative importance of mixing mechanisms under different environmental conditions is not fully understood. In particular, the contribution to plume mixing from bottom-generated shear stresses, referred to as tidal mixing, is rarely considered important relative to frontal and stratified shear (interfacial) mixing in surface advected plumes. The effect of different mixing mechanisms is investigated numerically on an idealized, tidally pulsed river plume with varying river discharge and tidal amplitudes. Frontal, interfacial, and tidal mixing are quantified via a mixing energy budget to compare the relative importance of each to the overall buoyancy flux over one tide. Results indicate that tidal mixing can dominate the energy budget when the tidal mixing power exceeds that of the input buoyancy flux. This occurs when the nondimensional number, $Ri_E R_0^{-1}$ (the estuarine Richardson number divided by the mouth Rossby number), is generally less than 1. Tidal mixing accounts for between 60% and 90% of the net mixing when $Ri_E R_0^{-1} < 1$, with the largest contributions during large tides and low discharge. Interfacial mixing varies from 10% to 90% of total mixing and dominates the budget for high discharge events with relatively weaker tides ($Ri_E R_0^{-1} > 1$). Frontal mixing is always less than 10% of total mixing and never dominates the budget. This work is the first to show tidal mixing as an important mixing mechanism in surface advected river plumes.

KEYWORDS: Ocean dynamics; Shear structure/flows; Turbulence; Mixing; Ocean models

1. Introduction

River plumes are created by the discharge of buoyant river water into the coastal ocean and create distinct hydrodynamic regions in the nearshore environment where water properties and dynamics are significantly influenced by freshwater. More than one-third of precipitation runoff from land travels by river to the ocean, where it is often mixed into the ocean via a river plume (Trenberth et al. 2007). River plumes are therefore responsible for the transportation and mixing of land-sourced pollutants, sediments, and organic matter into the ocean and so influence how these materials affect ecologically sensitive coastal zones. How tracers such as these are mixed into the ocean is related to physical mixing dynamics within a plume. Multiple mechanisms influence plume mixing, but their relative importance within different plumes and to each other has yet to be clarified.

Plume mixing is primarily controlled by stratified-shear instabilities, frontal processes, and wind forcing which create turbulent fluxes of buoyancy and momentum between the fresh, riverine discharge and salty, ambient ocean (e.g., Sherman et al. 1978; Ivey et al. 2008; Stacey et al. 2011). The

Oenotes content that is immediately available upon publication as open access.

Corresponding author: P. Spicer, preston.spicer@maine.edu

vertical turbulent buoyancy flux *B* is often estimated to quantify mixing. Point measurements from field data provide coarse estimates of *B* (MacDonald and Geyer 2004; MacDonald et al. 2007; Orton and Jay 2005; O'Donnell et al. 2008; Horner-Devine et al. 2013), but likely do not capture the heterogeneity in mixing across an entire plume. Those observations therefore begin a framework for estimating the fraction of dilution from freshwater to ocean salinity which each mixing process is responsible for.

To create a more comprehensive framework that quantifies net plume mixing and compares the relative importance of mixing processes in oceanic systems, recent studies have modeled mixing in terms of energy budgets (Winters et al. 1995; Wunsch and Ferrari 2004; MacCready et al. 2009). In a notable, simplified budget, Pritchard and Huntley (2006) use a potential energy model to argue that three main mechanisms are responsible for plume mixing: wind stress, tides, and frontal processes [later expanded upon by Horner-Devine et al. (2015, hereafter HHM15)]. The relative importance of those three mechanisms can be estimated if ε , the turbulent kinetic energy dissipation rate, is known within the plume. A few observational studies have applied the budget with limited measurements (Huguenard et al. 2016; Pritchard and Huntley 2006). The simplified budget lacks an inclusion of interfacial mixing, created by shear instabilities on the strongly stratified interface between ocean and plume. The budget also lacks a robust tidal mixing term, created by bottom-generated shear instabilities from tidal currents, which is broadly parameterized on current

^c Department of Civil and Environmental Engineering, University of Massachusetts Dartmouth, Dartmouth, Massachusetts d Department of Marine Sciences, University of Connecticut, Groton, Connecticut

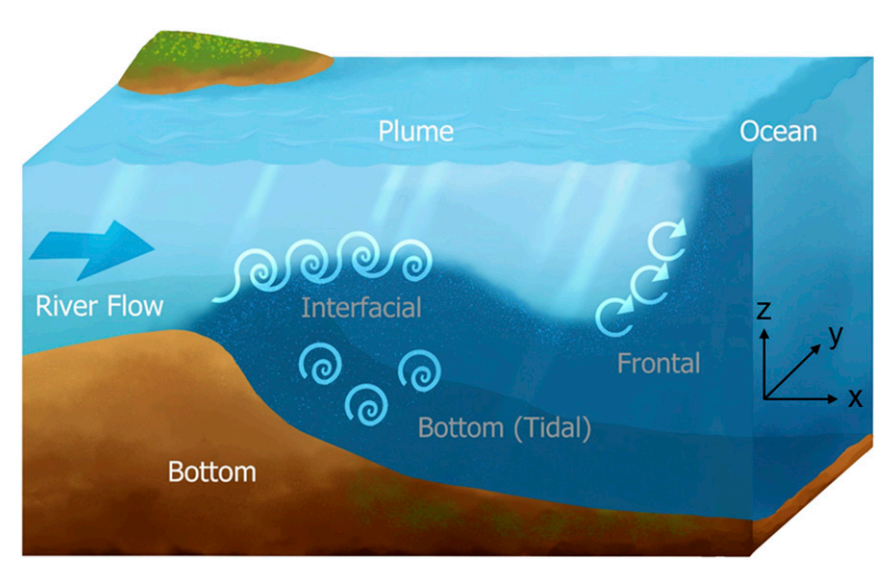


FIG. 1. Conceptual model of a river plume shows the major mixing mechanisms excluding wind. Input buoyancy from river discharge is mixed into shelf waters by bottom boundary (tidal), frontal, and interfacial mixing mechanisms. Darker blue indicates saltier ocean water and light blue represents fresher plume water.

magnitudes and an assumed stirring efficiency (both included with frontal mixing conceptually in Fig. 1). Interfacial mixing has been studied extensively and is shown to be important in radially spreading plume systems (Cole and Hetland 2016; MacDonald and Geyer 2004; MacDonald et al. 2007; Hetland 2005). Although tide-plume dynamics have been studied frequently, tidal mixing itself has largely been ignored but hypothesized to contribute in strongly tidal, shallow systems (HHM15; Fisher et al. 2002).

Surface advected plumes are influenced by tidal motions which can modify plume structure and mixing, particularly in meso/macrotidal systems (tidal ranges $> 2 \,\mathrm{m}$). Observations show plume fronts travel according to tidal direction and speed (O'Donnell et al. 2008; Rijnsburger et al. 2018), likely adjusting the importance of frontal and interfacial mixing with the tide. There are also indications that tidally modulated plumes can be subject to a type of tidal straining which periodically transforms plume stratification due to counterrotating tidal ellipses in the plume and bottom boundary layers (de Boer et al. 2006, 2008) and likely causes mixing at the plume base (Fisher et al. 2002). In Long Island Sound, past observations have shown tidally generated bottom stress can be substantial, generating mixing throughout the water column (Whitney et al. 2016; O'Donnell et al. 2014; Bowman and Esaias 1981), although its effect on mixing the strongly tidal Connecticut River plume within the Sound has not been quantified. Elsewhere, studies have connected tidally generated bottom stress to mixing and particle resuspension in plumes during low discharge, large tide events (Spahn et al. 2009; Nash et al. 2009). Bottom-generated tidal mixing and its relative importance to other mechanisms has yet to be quantified in surface plumes.

The simplified mixing energy budget of Pritchard and Huntley (2006) has not been evaluated for an entire plume throughout a tidal cycle, for plumes of different forcing

conditions, or with inclusion of nonparameterized interfacial and tidal mixing. The goal of this investigation is to evaluate the importance of interfacial, frontal, and tidal mixing on the net mixing budget of a river plume using an idealized numerical model and energy budget for an entire tidal cycle under varying conditions. The objectives of this work are to 1) quantify how the vertical mixing of plume water into shelf waters varies with tidal current magnitude and river discharge, and 2) diagnose the relative importance of each mixing mechanism to total mixing via the simplified energy budget within that parameter space. Similar to estuaries, plume forcing is closely connected to freshwater discharge and tides and so we identify variation in the mixing energy budget from those forcings. The remainder of this paper begins with a background on the numerical model configuration (section 2) and data analysis (section 3). A detailed account of the numerical simulation results is presented in section 4, outlining the importance of interfacial and tidal mixing on the net energy budget. Section 5 analyzes the conditions when tidal or interfacial mixing dominate the budget while section 6 discusses the relative importance of frontal mixing and the broader implications of this work. The main conclusions are presented in section 7.

2. Model

The simulations demonstrated here utilize the Regional Ocean Modeling System (ROMS) which is a free-surface, hydrostatic, primitive equation ocean model (Haidvogel et al. 2008). ROMS uses stretched, terrain following coordinates in the vertical direction and orthogonal coordinates in the horizontal direction. The domain is idealized so results may be extendable to other systems and features a long (15 km) and narrow (1500 m), shallow, constant-depth (5 m) estuary

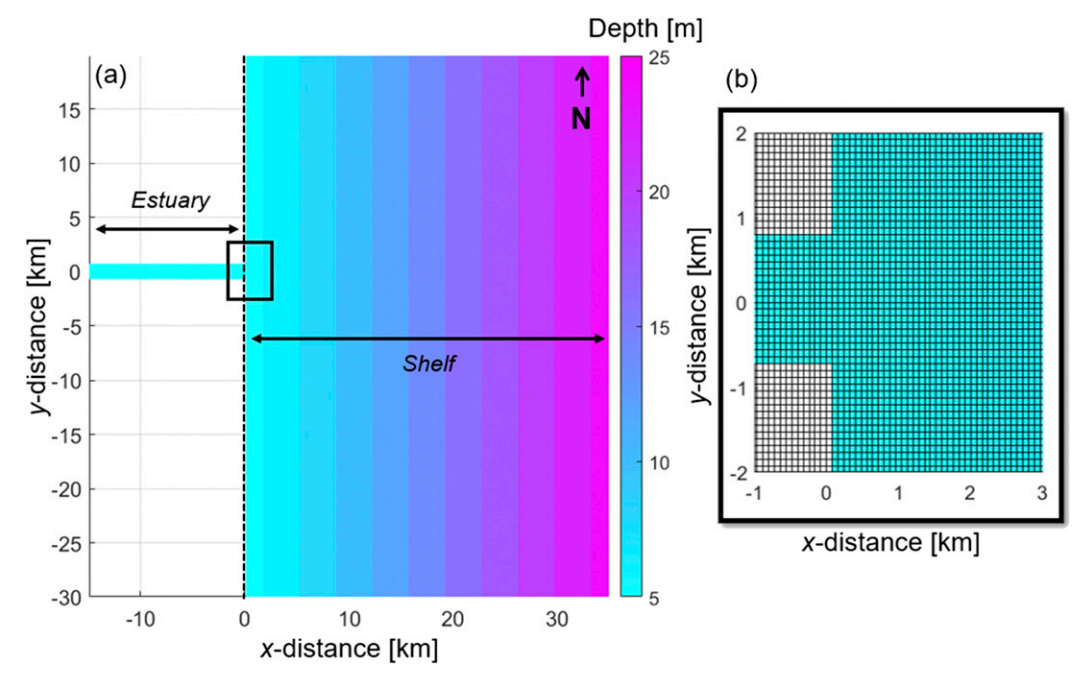


FIG. 2. (a) Plan view of bathymetry over the entire model domain, with the white area representing land and the dashed line separating estuary and coast from shelf. The vertical axis is the y distance (km) with 0 being in the middle of the estuary, and the horizontal axis is the x distance (km), with 0 being the estuary/shelf boundary. (b) Zoom-in of the mouth of the estuary, showing grid resolution and depth at the outflow.

attached to a linearly sloping shelf with a straight coastline (Fig. 2). The shelf depth increases to a maximum of 25 m at the eastern boundary. The oceanic section of the domain is 50 km long and 35 km wide, with square grid cells $80\,\mathrm{m} \times 80\,\mathrm{m}$ throughout. The model has 30 vertical layers, with increased resolution at the surface and bottom resulting in \sim 7 layers within the top 2 m of the water column over the entire domain.

The idealized model configuration broadly represents the Connecticut River plume in Long Island Sound, which has been studied extensively and is noted for significant tidal modulation (Garvine and Monk 1974; Garvine 1974; Garvine 1977; O'Donnell 1997; Jia and Whitney 2019). Long Island Sound features significant alongshore tidal currents due to geometry, which makes the Connecticut River plume an ideal system to study the effect of tides on a plume mixing budget. Although dimensions are based on the Connecticut River plume, tidally pulsed plumes with a narrow source (a mouth width smaller than the local deformation radius) will generally spread and mix similarly so results may be extrapolated to other systems.

River discharge is introduced on the western boundary of the 15-km estuary as freshwater (0 psu). Tides are forced by sea level as a sine wave near the M_2 period (12 h). The Coriolis parameter f was calculated for a latitude of 41°N, representative of the Connecticut River plume location. No winds are prescribed in any simulation to simulate simple environmental conditions and eliminate wind mixing from the analysis. A $5\,\mathrm{cm\,s^{-1}}$ constant downcoast current is forced at the upcoast oceanic boundary, which is typical of other idealized river

plume models and much slower than the tidal currents forced in these experiments (Hetland 2005; Cole and Hetland 2016).

Flather and Chapman conditions were applied at the open boundaries for the velocity and free surface, respectively, allowing fluid flow out of the domain (Flather 1976; Chapman 1985). Three-dimensional velocity components and tracers followed a radiation open boundary condition (Marchesiello et al. 2001). Vertical mixing was described by the $k-\varepsilon$ turbulence closure scheme (Umlauf and Burchard 2003) with Canuto A stability function formulation (Canuto et al. 2001). Horizontal and vertical tracer advections were calculated using the multidimensional positive definite advection transport algorithm (MPDATA; Smolarkiewicz and Grabowski 1990). Another advection scheme (U3H) was also applied to test the influence of numerical mixing on the analysis presented below. Ultimately, the choice of advection scheme created negligible differences (appendix C). The bottom boundary layer (BBL) model is applied for bottom stresses, with the nondimensional quadratic friction coefficient set to 0.003 which is typical of estuaries and coastal seas (Valle-Levinson 2010).

The model is initialized with a flat sea surface and a vertically uniform along-channel salinity gradient in the estuary from 0 psu at the upriver boundary to 32 psu in the oceanic domain. Each simulation was run for four full semidiurnal tidal cycles before analysis began on the fifth to allow for the estuarine circulation and plume to develop such that consecutive tidal pulses of freshwater onto the shelf exhibited similar horizontal and vertical spatial scales. Passive dye tracers (initial concentration = 1 kg m^{-3}) are released from the estuary mouth over the full width and depth at midflood

TABLE 1. Tidally averaged inflow parameters for all experiments. Columns (from left to right) show river discharge Q, tidal elevation amplitude $\eta_{\rm tide}$, Froude number Fr, Burger number S, baroclinic deformation radius R_d , the Rossby number R_o , estuary Richardson number ${\rm Ri}_E$, and ${\rm Ri}_E R_0^{-1}$.

$\overline{Q\ (\mathrm{m}^3\mathrm{s}^{-1})}$	$\eta_{\text{tide}}\left(\mathbf{m}\right)$	Fr	S	R_d (km)	R_o	Ri_E	$\mathrm{Ri}_E R_0^{-1}$
100	1.5	0.67	4.4	6.6	2.8	0.4	0.1
100	0.75	0.56	5.5	8.2	3.1	0.7	0.2
100	0	0.38	5.1	7.7	2.0	390	195
200	1.5	0.76	4.9	7.3	3.7	0.3	0.1
200	1.0	0.67	5.9	8.8	4.0	0.7	0.2
200	0.75	0.54	5.8	8.8	3.2	1.3	0.4
500	1.5	0.76	5.7	8.6	4.4	0.7	0.2
500	0.75	0.54	6.5	9.8	3.6	2.9	0.8
500	0.5	0.53	6.5	9.7	1.0	6.6	6.6
500	0	0.50	6.2	9.3	3.1	497	160
1000	1.5	0.77	6.3	9.4	4.8	1.2	0.3
1000	0.75	0.55	7.0	10.4	3.9	4.7	1.2
1000	0.5	0.54	6.9	10.4	1.2	10.2	8.5
1000	0	0.59	6.7	10.1	4.0	253	63

tide ($\eta = 0$ m and increasing) on the fifth tidal cycle to track the plume. A parameter space was chosen which encompasses microtidal to mesotidal plumes and relatively low to high discharges with the intent of creating plumes generally strongly tidally modulated. Tidal elevation amplitudes η_{tide} of 0, 0.75, and 1.5 m are each run with discharge rates Q of 100, 500, and 1000 m³ s⁻¹. An $\eta_{\text{tide}} = 0.5$ m is also run with $Q = 500 \text{ and } 1000 \text{ m}^3 \text{ s}^{-1} \text{ while } Q = 200 \text{ m}^3 \text{ s}^{-1} \text{ is run with tidal}$ amplitudes of 0.75, 1.0, and 1.5 m resulting in 14 experiments total (outlined in Table 1), which gave a realistic and reasonable range of values for the estuary inflow parameters described in the next paragraph. Figure 3 outlines the variation in horizontal plume extent under two different tidal amplitudes with a moderate discharge. For all runs, tidal elevations and velocities are in phase, not unlike a progressive Kelvin wave tide, and so maximum tidal current magnitudes occur during the minimum and maximum tidal elevations (Figs. 3a,c,e,g).

Tidally averaged estuary inflow parameters for each experiment are described in Table 1. Here, $R_d = \sqrt{g'h/f}$ is the baroclinic Rossby radius, which describes the length scale at which rotational effects become important over buoyancy, with $g' = g\Delta\rho/\rho_0$ being the reduced gravity at the estuary mouth, h is the depth at the mouth, g is the acceleration due to gravity, $\Delta\rho$ is the density anomaly of the inflow relative to ambient, and ρ_0 is the ambient density. The term $R_0 = U/fw$ is the mouth Rossby number with U being the mean velocity of inflow and W is the mouth width. Also, $S = R_d/W$ is the Burger number, and $Fr = R_0/S$ is the Froude number. Both R_0 and S are greater than unity for all runs, indicating that rotation does not dominate flow at the inflow and Fr < 1 for all cases, indicating that buoyancy influences plume evolution and the plume is surface advected (Yankovsky and Chapman 1997).

3. Methods

The mixing budget approach utilized in Pritchard and Huntley (2006) is based on a potential energy budget, with the

mechanical energy required to completely mix the water column being

$$\phi = \frac{1}{\eta + H} \int_{-H}^{\eta} gz(\overline{\rho} - \rho) dz, \qquad (1)$$

where η is the free surface elevation, H is the bottom depth, z is the vertical coordinate, and $\bar{\rho}$ is the vertical mean density. Equation (1) quantifies stratification in the water column (Burchard and Hofmeister 2008; HHM15) and is used in this work to define the total energy required to completely mix a river plume with ambient waters. We note that ϕ can be misleading at times in highly stratified systems, as the location of a two-layer interface relative to the middepth can slightly change ϕ (MacDonald and Horner-Devine 2008). Regardless, Eq. (1) was deemed appropriate as a simple metric to compare the relative magnitude of stratification between plumes.

Similar to HHM15, we express each mixing energy via the vertical turbulent buoyancy flux B (W kg $^{-1}$), which allows for a determination of mixing power [in watts (W)] after consideration of the density of seawater and depth and area B acts over. The dye release beginning on the fifth tidal cycle was used as the start point for the budget analysis on all experiments and ended when inestuary dye was cut off from the shelf. The dye distinguishes ambient stratification from the tidal plume. The buoyancy flux B was calculated at all grid points in that plume allowing for a complete view of plume mixing in space and time. The vertical turbulent buoyancy flux can be calculated as

$$B = -\frac{g}{\rho_0} K_{\rho} \frac{\partial \rho}{\partial z},\tag{2}$$

where K_{ρ} is the vertical eddy diffusivity and ρ is the density at vertical coordinate z. Equation (2) was determined using the ROMS output of eddy diffusivity and density, which allowed for the simplified mixing energy budget (Pritchard and Huntley 2006) to be resolved.

The total mixing power M within the dye-tracked plume was calculated at each time step using a volume integral of B throughout the plume, which we explicitly state here as

$$M = \rho_0 \sum_{i=0}^{n} A_i \int_{d_n}^{\eta} B_i \, dz, \tag{3}$$

where n is the number of horizontal grid points in the plume, A_i is the horizontal area of each cell (80 m × 80 m) in the plume at each grid point i, d_{p_i} is the plume depth at each point and is considered the depth where dye concentration falls below 10^{-2} kg m⁻³, and B_i is the buoyancy flux at each grid point. The dye threshold chosen produced the most realistic plume boundaries both vertically and horizontally based on in-estuary dye releases as it matched the outer edge of the plume surface salinity field and fell near the largest vertical gradients in dye within the water column. Spatial limits to integration in Eq. (3) are based on Eq. (1): i.e., ϕ must be greater than 0 at a given dye-tracked plume coordinate and d_{p_i} cannot be equal to the bottom depth (indicating a new, surface-advected plume exists) else $\begin{bmatrix} n \\ i \end{bmatrix}$ is set to zero.

surface-advected plume exists) else $\int_{d_{p_i}}^{\eta} B_i$ is set to zero. The frontal mixing power $M_{\rm FR}$ was calculated by summing grid volume integrals of B along a narrow band on the perimeter of the plume considered the frontal region:

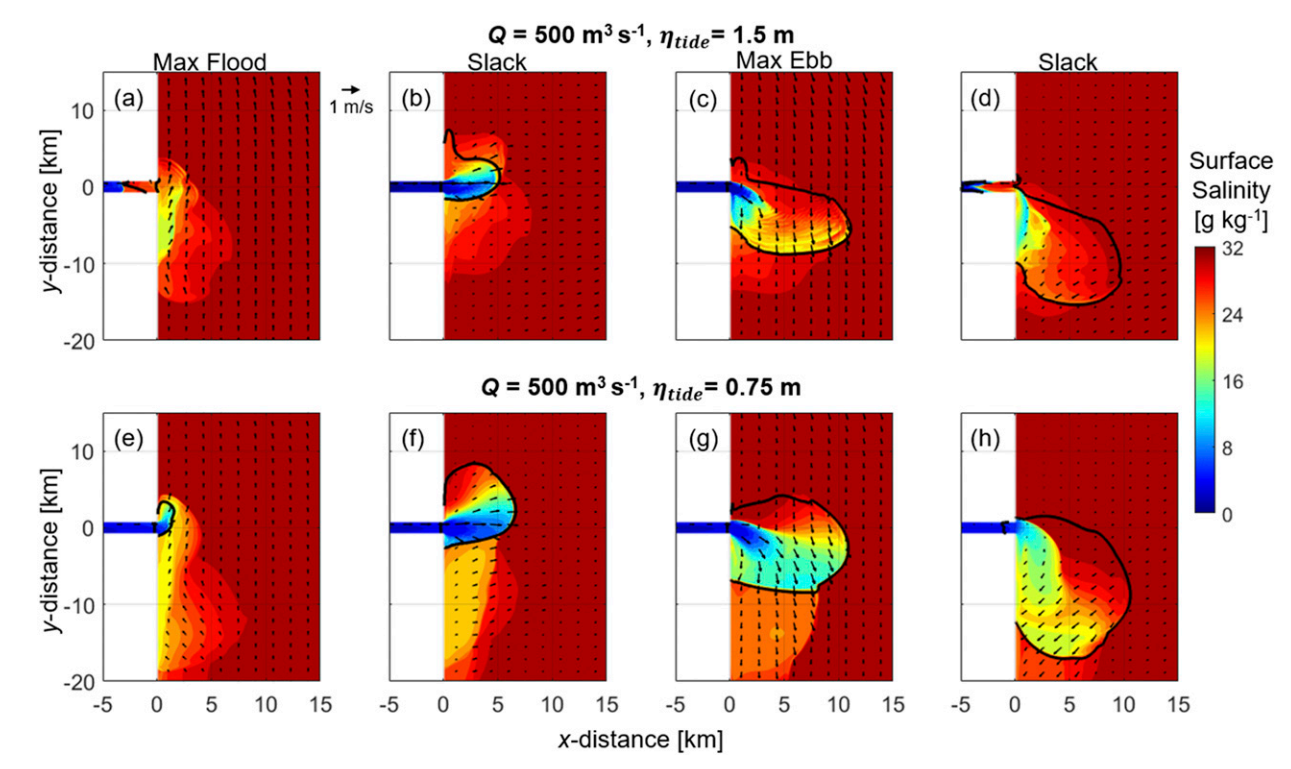


FIG. 3. Surface salinity distribution over the fifth tidal cycle for two moderate discharge $(Q = 500 \,\mathrm{m}^3 \,\mathrm{s}^{-1})$ runs: progression from maximum flood tidal currents to the slack tide after ebb (a)–(d) for $\eta_{\mathrm{tide}} = 1.5 \,\mathrm{m}$ and (e)–(h) for $\eta_{\mathrm{tide}} = 0.75 \,\mathrm{m}$. The x and y axes are x and y distances, respectively. The thick black line bounds the plume being analyzed according to dye released at the mouth. Surface current magnitude and direction are denoted by black arrows.

$$M_{\rm FR} = \rho_0 \sum_{i=0}^{j} A_i \int_{d_i}^{\eta} B_i \, dz \,, \tag{4}$$

where j is the number of horizontal ρ grid points in the frontal zone and d_{f_i} is the frontal depth at each point [determined with dye like Eq. (3)]. The total area over which the front is active $(\sum_{i=0}^{J} A_i)$ is estimated in different ways in this work. Former research has simply estimated a "frontal distance" over which frontal mixing occurs based on conceptual dimensions, satellite imagery, and frontal propagation speeds (Huguenard et al. 2016; Pritchard and Huntley 2006; O'Donnell et al. 2008). In this work, j was liberally estimated based on the horizontal gradient of surface dye, with any grid point containing a gradient larger than 10^{-3} kg m⁻⁴ considered as the frontal zone. Gradients of that magnitude only occurred at the plume-ambient boundary and resulted in large frontal distances ranging from the grid length (80 m) to multiple hundreds of meters (up to 300 m). Former estimates of frontal length scales produced values of similar magnitude (Huguenard et al. 2016). Estimates were also made based on salinity gradients and setting a constant length scale to compare results. We found the different values estimated for frontal length scale in this work had little impact on the results and is discussed further in section 6c.

In this work, we present a new method to distinguish the contributions of interfacial and tidal mixing to the plume energy budget in a robust, nonparameterized manner compared to previous studies. To quantify the mixing energies, it was

important to distinguish the two mechanisms from each other, as they interact with the plume over the same regions (Fig. 1). We followed the estuarine method of Ralston et al. (2010), in which there are conditions (appendix A) that determine how to separate tidal and interfacial mixing which can slightly modify the structure of the following equations. We present Eq. (5) with the assumption that there is no tidal mixing (condition 1, appendix A) whereas Eq. (7) assumes both tidal and interfacial mixing (condition 2, appendix A). This was considered the most logical way to present the method and is important to note here.

When isolated from other mechanisms, buoyancy flux from shear instabilities at the interface peaks within the plume layer and approaches zero at the plume base and surface, conceptually depicted in Fig. 4a (Yuan and Horner-Devine 2013). In this case, interfacial mixing power $M_{\rm IF}$ can be calculated by integrating B over the plume layer (excluding the frontal zone), similarly to Eq. (3):

$$M_{\rm IF} = \rho_0 \sum_{i=0}^{k} A_i \int_{d_{p_i}}^{\eta} B_i \, dz \,, \tag{5}$$

where k is the number of horizontal ρ grid points in the non-frontal portion of the plume. The total area of the nonfrontal portion of the plume $(\sum_{i=0}^k A_i)$ used to determine k was considered the area bounded by surface dye concentrations greater than 10^{-2} kg m⁻³ with the total frontal area subtracted.

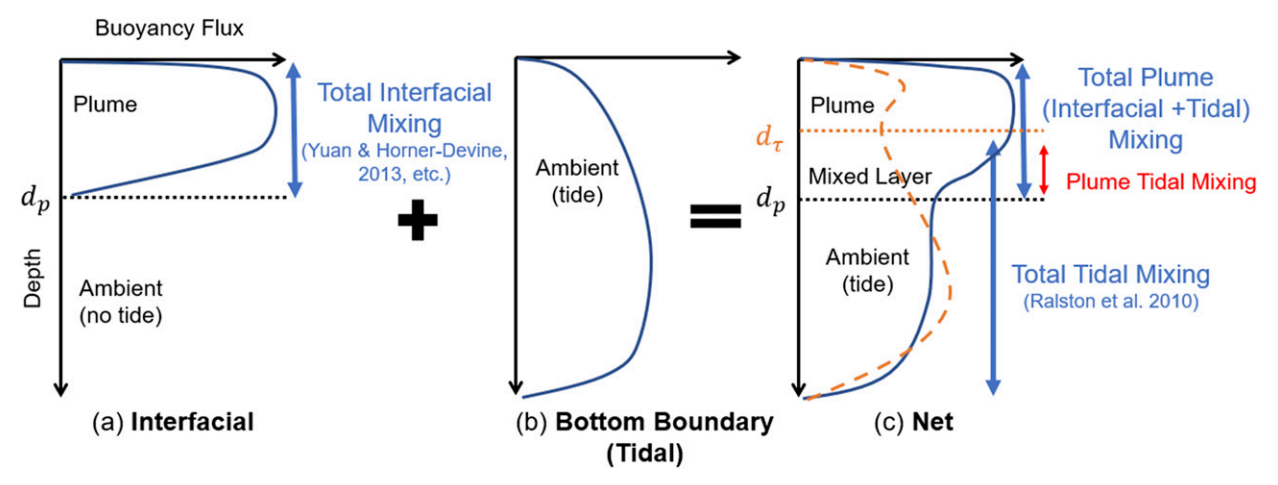


FIG. 4. Conceptual diagram of vertical structure of turbulent buoyancy flux, B (blue lines), for (a) only interfacial plume mixing, (b) only tidal mixing of ambient stratification, and (c) the combination of interfacial and tidal mixing. A profile of shear stress τ (dashed orange) is shown in (c). Vertical axis on each plot is nondimensional depth and horizontal is nondimensional B and/or τ . Plume depth d_p and shear stress local minimum depth d_{τ} are labeled.

Equation (5) is complicated when bottom-boundary mixing from tidal currents is introduced. Tidal mixing of ambient shelf water without the existence of a plume results in a peak B near the bottom of the water column, decaying to zero at the surface and bottom (Fig. 4b). When plume stratification is introduced, near-surface tidal B is damped, though some portion of tidal buoyancy flux may still contribute to mixing the plume water. Conceptually, this creates a nonzero local minimum in B in the mixed layer at the plume base, shown in Fig. 4c (Ralston et al. 2010). Integrating B from the surface to the plume base is no longer quantifying strictly interfacial mixing, but rather interfacial mixing combined with a fraction of tidal mixing which influences the plume. To separate the two mechanisms, we apply the method of Ralston et al. (2010) to river plumes and distinguish tidal mixing from interfacial via the magnitude of the vertical component of shear stress τ :

$$\tau = K_m \sqrt{\left(\frac{\partial u}{\partial z}\right)^2 + \left(\frac{\partial v}{\partial z}\right)^2},\tag{6}$$

where K_m is the vertical eddy viscosity output from the turbulence closure, and u and v are the east—west and north—south components to current velocities, respectively. Similar to B, local maxima in shear stress can exist near bottom and within the plume layer when both interfacial and tidal mixing are important, with τ sometimes offset from B (Fig. 4c). The local minimum (d_{τ}) between the two maxima is taken as the boundary between the mixing mechanisms [Fig. 4c, with mixing above d_{τ} being only interfacial whereas below is tidal, as described in Ralston et al. (2010)]. Whenever d_{τ} is shallower than d_{p_i} , tidal mixing and interfacial mixing both can be considered influential to total plume mixing and M_T is calculated as

$$M_{T} = \left(\rho_{0} \sum_{i=0}^{k} A_{i} \int_{d_{p_{i}}}^{\eta} B_{i} dz\right) - \left(\rho_{0} \sum_{i=0}^{k} A_{i} \int_{d_{\tau_{i}}}^{\eta} B_{i} dz\right), \tag{7}$$

where d_{τ_i} is the local minimum in shear stress at each grid point *i*. Conceptually, the left-hand term in Eq. (7) is the total mixing within the plume layer (Fig. 4c) while the right-hand term is mixing from interfacial instabilities only (Fig. 4a).

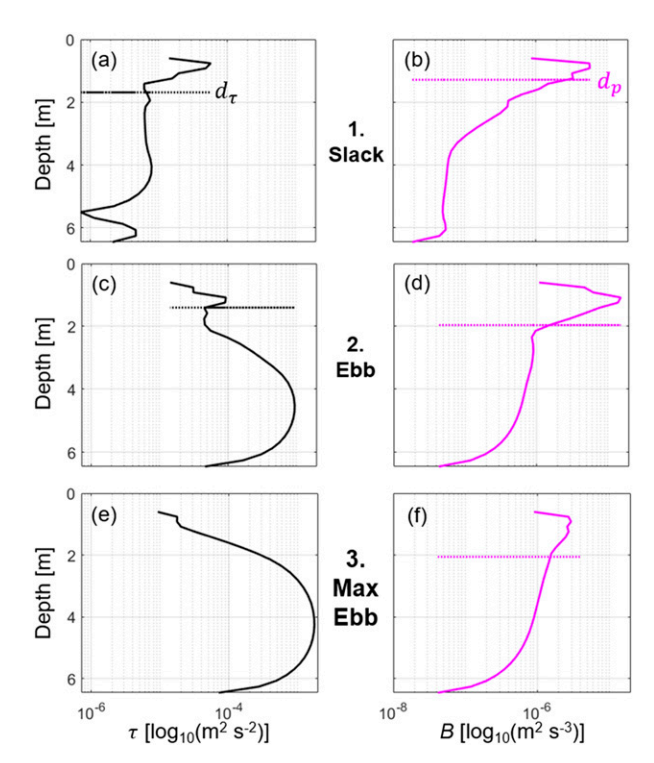


FIG. 5. Profiles of (a),(c),(e) shear stress τ and (b),(d),(f) vertical turbulent buoyancy flux B from the $Q = 500 \,\mathrm{m}^3 \,\mathrm{s}^{-1}$, $\eta_{\mathrm{tide}} = 0.75 \,\mathrm{m}$ run taken at $x = 3 \,\mathrm{km}$, $y = 0 \,\mathrm{km}$. Profiles were taken at 1) slack tide, 2) mid-ebb, and 3) max ebb and correspond to each mixing calculation condition outlined in appendix A. Vertical axis on each plot is depth and horizontal is B and/or τ . Plume depth d_p and shear stress local minimum depth d_τ are labeled if they are present.

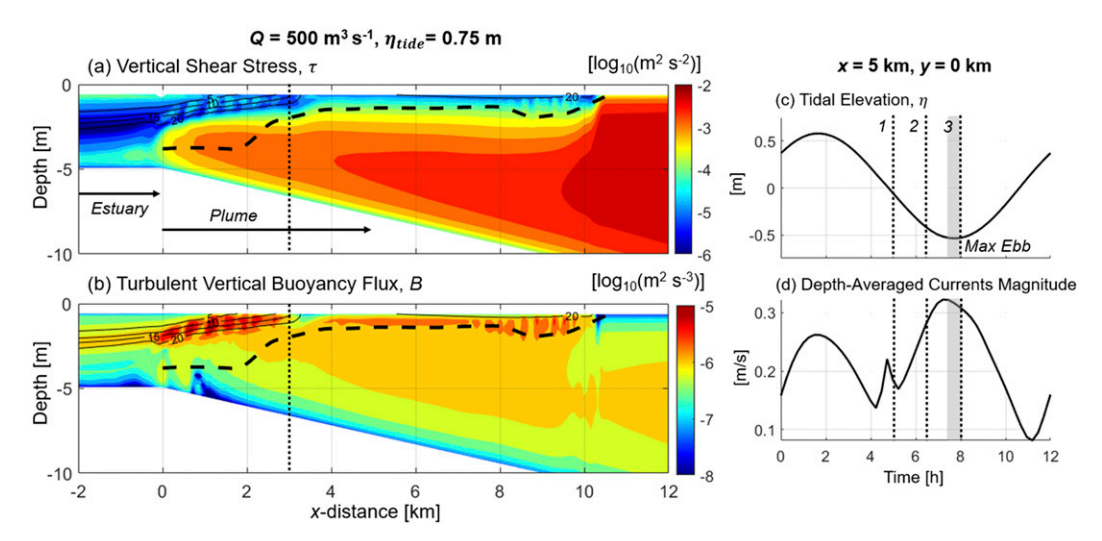


FIG. 6. Contours of (a) shear stress τ and (b) vertical turbulent buoyancy flux B during max ebb for the $Q = 500 \,\mathrm{m}^3 \,\mathrm{s}^{-1}$, $\eta_{\mathrm{tide}} = 0.75 \,\mathrm{m}$ run (see Fig. 3g) at $y = 0 \,\mathrm{km}$. Both color bars are on a \log_{10} scale. Contours of density anomaly σ_{θ} (kg m⁻³) are shown as solid black lines and labeled, while the plume depth according to the dye release is marked with a dashed black line. The vertical axes are depth, and the horizontal axes are x distance. Plots of the (c) tidal elevation η and (d) depth-averaged currents are also shown at a midplume location ($x = 5 \,\mathrm{km}$, $y = 0 \,\mathrm{km}$) with max ebb [shown in (a) and (b)] shaded in gray. The dashed lines in (a) and (b) denote the location of the profiles from Fig. 5 whereas in (c) and (d) they mark the times at which profiles 1, 2, and 3 were taken.

When Eq. (7) is applicable, Eq. (5) must be modified to mimic the right-hand term in Eq. (7) (condition 2, appendix A). When d_{τ_i} is found deeper than d_{p_i} , Eq. (7) is not applicable and M_T must equal zero (condition 1, appendix A), and when there is no d_{τ_i} there is no local minimum and all plume mixing is considered tidal (Ralston et al. 2010) (condition 3, appendix A). A set of B and τ profiles from a moderate tide and discharge are shown to exemplify each of these conditions in the data (Fig. 5). In this case, conditions 1 (Figs. 5a,b), 2 (Figs. 5c,d), and 3 (Figs. 5e,f) occur within the same plume as tidal currents increase on ebb (Figs. 6c,d). Considering tidal mixing does not distinguish between the frontal region and interior of the plume, the same conditions apply in the frontal zone (appendix A). Tidal mixing below the plume layer was evaluated and considered negligible in its effect on Eq. (7) (appendix B), justifying the integration to d_{p_i} . The method outlined above was corroborated by turning bottom friction on and off in the model and quantifying tidal mixing as the difference between Eq. (5) with friction and Eq. (5) without friction. That test was used on most cases and produced nearly identical results (not shown) to those presented in the next section. The nature of the equations presented above is such that all mixing power terms (M_F, M_{IF}, M_T) always sum to the total plume mixing power M. Each term is comprised of some volume integral of B within the total plume volume, used to determine M, and so result in a closed mixing budget as their summed regions are neither greater than or less than the total plume region.

4. Results

All experiments exhibit a plume front which exits the estuary near maximum flood currents, with the highest discharge cases just prior to max flood (Fig. 3e) and the lowest discharges just after max flood (Fig. 3a). The plume rotates from north to south with the change in tidal phase after exiting the estuary (Figs. 3b,c,f,g). A salinity intrusion front enters the estuary during flood on all runs, with the intrusion extent dependent on discharge and tidal magnitude (Fig. 3d). The estuary is a salt wedge in all experiments [Fr > 0.07 from Geyer and MacCready (2014)] and a plume lift-off point occurs near the mouth of the estuary where the bottom begins sloping to the shelf.

a. Plume structure

A vertical cross section of shear stress, density anomaly, and turbulent buoyancy flux is shown in Fig. 6 to conceptualize the vertical plume mixing structure during low water when ebb tidal currents are strongest. The near-field plume, where generally the strongest interfacial mixing occurs (HHM15), is arbitrarily defined as the region from approximately x = 0 to 4 km, as the most intense in-plume mixing occurs there ($\varepsilon \sim$ $10^{-4.5} \,\mathrm{m^2 \, s^{-3}}$ and $B \sim 10^{-5} \,\mathrm{m^2 \, s^{-3}}$ at 1–2-m depth, Fig. 6). Shear stress peaks in the midwater column below the plume layer from tidally generated bottom shear ($\tau \sim 10^{-3}\,\mathrm{m}^2\,\mathrm{s}^{-2}$ at 3-5-m depth, Fig. 6b) and generally features another local maximum in the near-field plume layer from interfacial instabilities ($\tau \sim 10^{-4}\,\mathrm{m^2\,s^{-2}}$ when $\sigma_{\rho} = 5$ –20 kg m⁻³ at 0.5–2-m depth and x < 4 km, Fig. 6b). The multiple maxima in stress suggest interfacial and tidal mixing could both be influential in the near field. Seaward of the near field, no notable areas of enhanced τ exist in the plume layer, indicating tidal mixing could be more important. This is corroborated by the profile in Fig. 5e (corresponds to dashed line in Figs. 6a,b) where no d_{τ} exists and implies tidal mixing is likely dominant during max

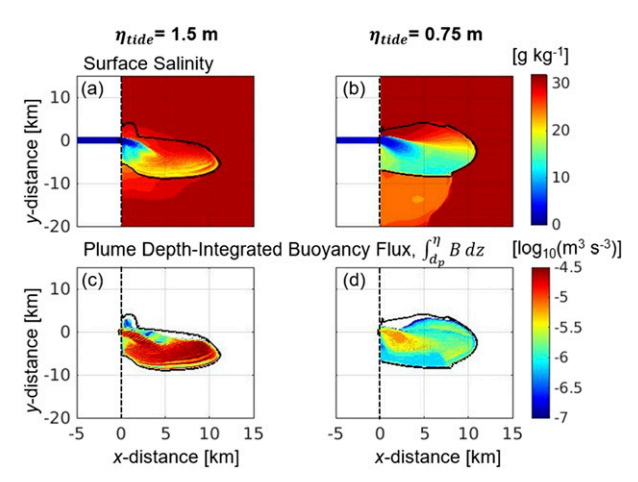


FIG. 7. Contours of (a),(b) surface salinity and (c),(d) plume depth integrated vertical turbulent buoyancy flux (m³ s $^{-3}$) on a log₁₀ scale for two $Q = 500 \,\mathrm{m}^3 \,\mathrm{s}^{-1}$ runs at max ebb. (left) The $\eta_{\mathrm{tide}} = 1.5 \,\mathrm{m}$ run (Fig. 3c), (right) the $\eta_{\mathrm{tide}} = 0.75 \,\mathrm{m}$ run (Fig. 3d), with (d) showing the horizontal variation of Fig. 5. Plume boundaries are denoted in each panel as a solid black line. Vertical axes are y distance (km), and horizontal axes are x distance (km). Warmer colors in (c) and (d) denote more vertical mixing.

ebb seaward of the near field. Elevated buoyancy flux values throughout the plume generally occur near or above d_p ($10^{-5.5}$ – 10^{-5} m² s $^{-3}$ at 1–2-m depth, Fig. 6b) illustrating intense mixing is occurring in the plume, regardless of if interfacial-generated shear stress exists. The variable spatial structure of shear stress and buoyancy flux in a moderate tide and discharge plume shows shear and stratification patterns differ, which therefore implies variability in mixing over the interior plume during peak tidal currents.

The variation between tides in each plume is most notable in the horizontal structure of surface salinity and total depthintegrated B within the plume layer (Fig. 7). For a large tide $(\eta_{\text{tide}} = 1.5 \,\text{m})$ surface salinity is more mixed with ambient salinity (>20 psu relative to 32 psu ambient) beyond the near field (>4 km in x distance in Fig. 7a) during maximum ebb currents. During a moderate tide ($\eta_{\text{tide}} = 0.75 \,\text{m}$), fresher surface water (>12 psu) exists beyond the near field simultaneously (x > 4 km, Fig. 7b). There is also spatial variation in total mixing within the plume layer between large and moderate tides with the larger tide case showing peak B throughout the plume $(\int_0^{d_p} B dz \sim 10^{-5.5} - 10^{-4.5} \text{ m}^{\frac{3}{3}} \text{ s}^{-3},$ Fig. 7c) relative to the moderate tide case, where enhanced $B (\int_0^{d_p} B dz \sim 10^{-5.5} \,\mathrm{m}^3 \,\mathrm{s}^{-3}$, Fig. 7d) was focused in the near field. The differences in mixing energy terms between each tide and discharge is outlined next to further elucidate the importance of each mechanism.

b. Intratidal variation in mixing terms

During the highest river discharge cases ($Q=1000\,\mathrm{m}^3\,\mathrm{s}^{-1}$), the tidal maximum in total potential energy (spatial sum of ϕ) was smallest and occurred earliest (9 MJ, hour 6.5 in Fig. 8a) for the largest tide ($\eta_{\mathrm{tide}}=1.5\,\mathrm{m}$) relative to the moderate ($\eta_{\mathrm{tide}}=0.75\,\mathrm{m}$) and no tide ($\eta_{\mathrm{tide}}=0\,\mathrm{m}$) experiments (11 and 20 MJ at

hours 8 and 12, respectively, in Fig. 8a). Larger tides create more mixing within the water column, which limits stratification from increasing over the tidal cycle such as when no tide is present, and the plume continually expands over the shelf. As tidal amplitude increases, stratification levels out, then decreases during maximum ebb currents, indicating an enhanced influence of tides on plume mixing.

Mixing power terms $M_{\rm IF}$ and M_F maximize during larger tides then decrease with tidal amplitude similar to M, with all cases peaking prior to max ebb. The large tide case is the most significant, with maxima of 3 and 0.15 MW near hour 7 (for $M_{\rm IF}$ and M_F , respectively) followed by the moderate tide peaking at 1.8 and 0.06 MW near hour 6 (for $M_{\rm IF}$ and M_F , respectively) (Figs. 8b,c). For all tides, maximum $M_{\rm IF}$ and M_F occur prior to max ebb, when near maximum buoyancy is input to the plume (Fig. 8a), but tidal currents have not yet peaked. The no-tide cases exhibited a small linear increase over the 12-h duration for $M_{\rm IF}$ and was near constant for M_F , both of which were small relative to the tidal plumes (Figs. 8b,c).

Tidal mixing power peaks near max ebb and increases more significantly with tidal amplitude relative to $M_{\rm IF}$ and M_F . Maximum M_T for the large tide clearly dominates the other terms for that tidal case (22 MW at hour 8 in Fig. 8d). Maximum M_T then decreases by nearly 5 times for the moderate tide and occurs slightly later (4 MW at hour 9 in Fig. 8d). Both tidal runs exhibit peak M_T near max ebb when tidal currents are strongest beneath the plume. When no tide is present, M_T is zero, as expected. Tidal mixing power M_T exhibits the largest variability in maxima over different tides relative to other mixing terms and notably dominates all mixing terms for the largest tide.

Under moderate discharge conditions ($Q = 500 \,\mathrm{m}^3 \,\mathrm{s}^{-1}$), nearly identical patterns in each potential energy and power term are evident but are weaker in magnitude (Fig. 9). For the moderate tide, peak M_T is comparable to the $Q = 1000 \,\mathrm{m}^3 \,\mathrm{s}^{-1}$ counterpart (4 MW at hour 8.5 in Fig. 9d), whereas for the large tide peak M_T is significantly less (13 MW at hour 8.5 in Fig. 9d) and exemplifies how a combination of increased tides and discharge are needed for maximized M_T . Smaller discharges ($Q = 200 \,\mathrm{and} \,Q = 100 \,\mathrm{m}^3 \,\mathrm{s}^{-1}$) yield similar trends to those outlined above (not shown).

c. Simplified budget: Relative importance of terms

To synthesize all results and quantify the relative importance of each mixing mechanism through the budget, the experiments were evaluated with nondimensional numbers encompassing both tides and discharge. The estuarine Richardson number, Ri_E, (Fischer 1972), is used as a basis and is defined as

$$Ri_E = \frac{g'Q}{Wu_{\text{tide}}^3},\tag{8}$$

with Q being the freshwater discharge and $u_{\rm tide}$ the tidal current magnitude in the estuary. ${\rm Ri}_E$ has been linked to vertical structure and bottom-generated sediment transport in plumes (Nash et al. 2009; Spahn et al. 2009). ${\rm Ri}_E$ can physically be interpreted as the ratio of freshwater transport to tidal power available for turbulent mixing in the estuary. Plumes have also

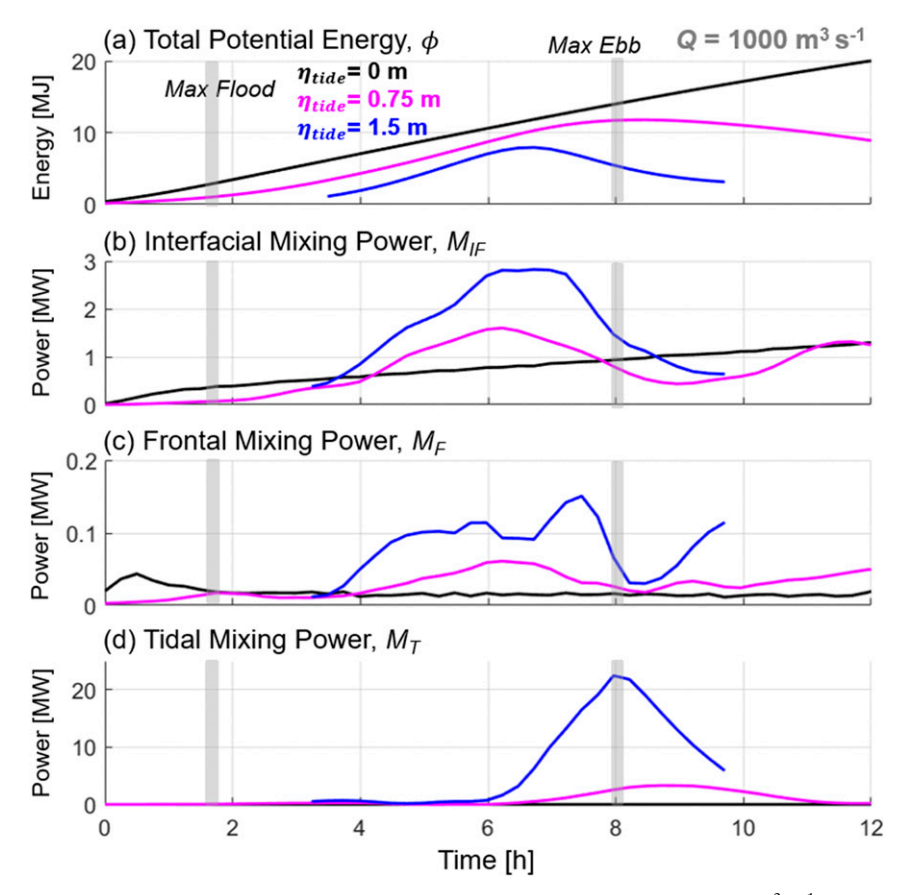


FIG. 8. Time varying instantaneous energy budget terms for three $Q=1000\,\mathrm{m}^3\,\mathrm{s}^{-1}$ experiments. (a) Total plume potential energy ϕ , (b) interfacial mixing power M_{IF} , (c) frontal mixing power M_F , and (d) tidal mixing power M_T . Horizontal axes are time in hours. Blue lines denote $\eta_{\mathrm{tide}}=1.5\,\mathrm{m}$ runs, magenta are $\eta_{\mathrm{tide}}=0.75\,\mathrm{m}$ runs, and black are $\eta_{\mathrm{tide}}=0\,\mathrm{m}$ runs. Max flood and ebb tidal currents are marked with gray shading.

been defined by the dimensional plume-to-cross-flow length scale (Jones et al. 2007): $L_x = g'Q/u_a^3$, where u_a is the ambient velocity. The length L_x is the scale of influence of the input buoyancy arrested by a cross-flow (i.e., how far offshore a plume spreads before a cross-plume current arrests spreading). The spreading of river plumes determines the radial expansion of the near and midfield plume and is defined as the stretching of a water parcel as it advects through a flow field from strain acting perpendicular to the parcel. In equation form, this lateral spreading is $\delta = \partial v/\partial v$ for local flow is in the x direction (Hetland and MacDonald 2008). To arrest spreading implies that lateral straining is minimized, and the radial expansion of a plume is slowed or stopped. Therefore, in this application L_r is the length scale of the tidal plume arrested by tidal cross-flow on the shelf. Thus, Ri_E can also be interpreted as the ratio of the length L_x to the mouth width which traditionally scales in size with the near-field plume, assuming $u_a = u_{\text{tide}}$.

Some estuary-plume systems exhibit much different magnitudes in tidal currents once outside the estuary, and the tidal mixing implied by Ri_E may not apply beyond the mouth. To make a stronger connection between tidal mixing outside the estuary and a plume length scale, we multiply Ri_E by the

inverse of the Rossby number and quantify u_{tide} as an average of tidal currents beneath the plume on the shelf:

$$Ri_{E}R_{0}^{-1} = \frac{g'Q}{Wu_{\text{tide}}^{3}} \frac{W}{R_{I}} = \frac{g'Q}{R_{I}u_{\text{tide}}^{3}},$$
 (9)

where the plume inertial radius is $R_I = U/f$ and has been found to scale with plume spreading (Kakoulaki 2015; Kakoulaki et al. 2020). Physically, the nondimensional Eq. (9) modifies our interpretation of the estuary Richardson number to be the ratio of freshwater transport to tidal power available for turbulent mixing *under the plume*, with the plume tidal power now scaling with plume spreading. We believe this formulation is more suitable for the full extent of the tidal plume than the mouth width scaling applied in Eq. (8).

The Ri_E and Ri_E R_0^{-1} values were calculated for each experiment then averaged over the 12-h tidal period (denoted with $\langle \rangle$) (Table 1). The ratio of each cumulative power term to the cumulative total power [Eq. (3)] over the time the plume is attached to the estuary ($\sum M_x/\sum M$, with x representing the various mechanisms) was then compared to $\langle \text{Ri}_E R_0^{-1} \rangle$ to identify the relative importance of each mixing mechanism to

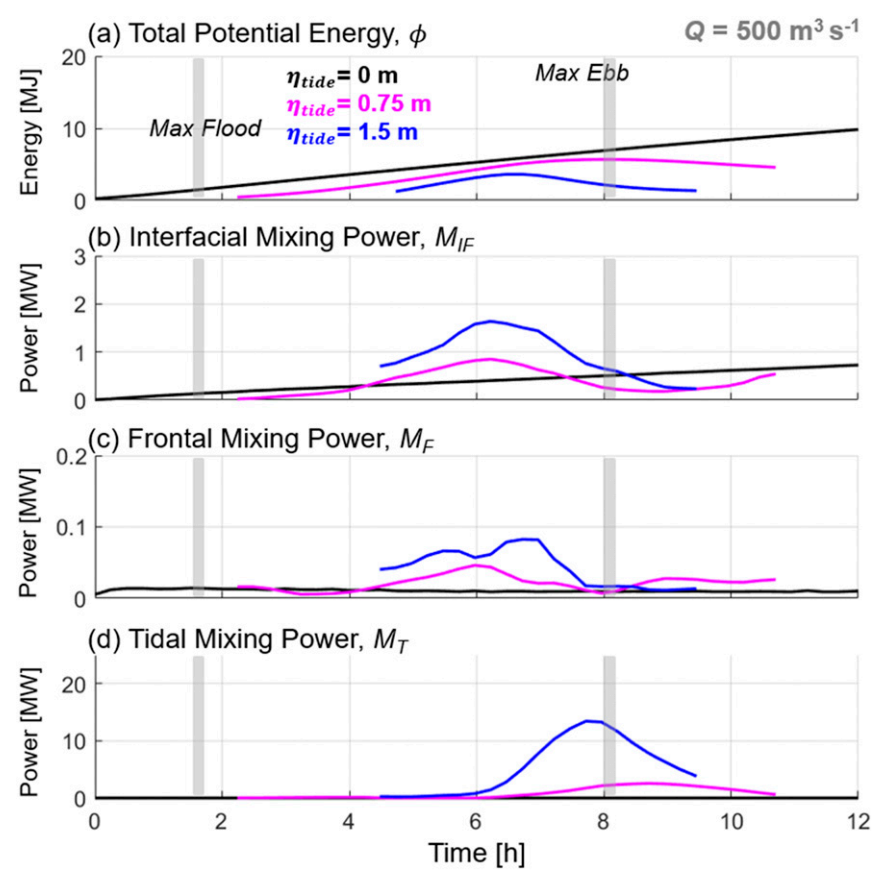


FIG. 9. As in Fig. 7, but for $Q = 500 \,\mathrm{m}^3 \,\mathrm{s}^{-1}$ experiments.

total plume mixing over the tidal plume's duration (Fig. 10). For all $\langle Ri_E R_0^{-1} \rangle < 1.3$, tidal mixing power is the dominant mechanism in the energy budget, ranging from 55% to 90% of the total mixing energy, with interfacial mixing accounting for 10%–40% of the budget. Based on Eq. (9), $\langle Ri_E R_0^{-1} \rangle = 1$ marks the theoretical threshold between a plume generally uninfluenced by tidal cross flow (>1) and one that is arrested and significantly mixed by the tidal cross flow (<1). Cases when L_x is on the order of or larger that R_I , other mechanisms may be dominant in the mixing budget ($\langle Ri_E R_0^{-1} \rangle > 1$), which is near the 1.3 observed here. Similar to theory, these results show when $\langle Ri_E R_0^{-1} \rangle > 1.3$ mixing energy dominance shifts to interfacial mixing (ranging from 55% to 95%) and tidal mixing decreases in importance from 40% to less than 5% of total mixing. For all cases, frontal mixing contributes the least to total mixing (<10%). Collectively, Fig. 10 shows plumes with relatively enhanced tidal influence (smaller $\langle Ri_E R_0^{-1} \rangle$) experience a significant M_T , whereas plumes with enhanced freshwater influence (larger $\langle \text{Ri}_E R_0^{-1} \rangle$) experience a more significant M_{IF} . Frontal mixing has a slight increase in importance for larger $\langle Ri_E R_0^{-1} \rangle$ but to a negligible degree relative to interfacial mixing.

5. Analysis

River plume dilution controlled by tidal mixing has not been investigated before in surface advected plumes. Although the influence of interfacial mixing is not always dominant in these experiments, the relative importance of the mechanism (10%–40% for tidal runs) is quite close to some of the more robust estimates of interfacial near-field mixing in situ (MacDonald et al. 2007; Kilcher et al. 2012). These results help advance our understanding of both mechanisms. To better grasp how tidal mixing can become so large relative to the other mixing terms, we explore estuary and plume dynamics associated with the estuarine Richardson number and plume lengths scales, then decompose the spatial variability of mixing dynamics for the experiments featuring the largest M_T .

a. Tidal versus interfacial mixing: Ri_E and R_o

Prior research has made the connection between deeper, bottom-boundary interacting plumes and tidal mixing through Ri_E . Nash et al. (2009) found that plume salinity, thickness, and mixing at the base all increase as Ri_E decreases (i.e., tidal currents increase). Essentially, a strongly sheared estuarine outflow creates a more mixed, deeper-reaching plume that is prone to interact with the bottom-boundary layer. Consistent with Nash et al. (2009), for all discharges, increasing tidal amplitudes subsequently decreased $\langle Ri_E \rangle$ and our spreading-scaled $\langle Ri_E R_0^{-1} \rangle$, implying an enhanced mixed layer at the plume base within the estuary and over the shelf. The maximized $\sum M_T / \sum M$ that corresponded to those $\langle Ri_E \rangle$ and $\langle Ri_E R_0^{-1} \rangle$ values quantified the expansion of the mixed layer.

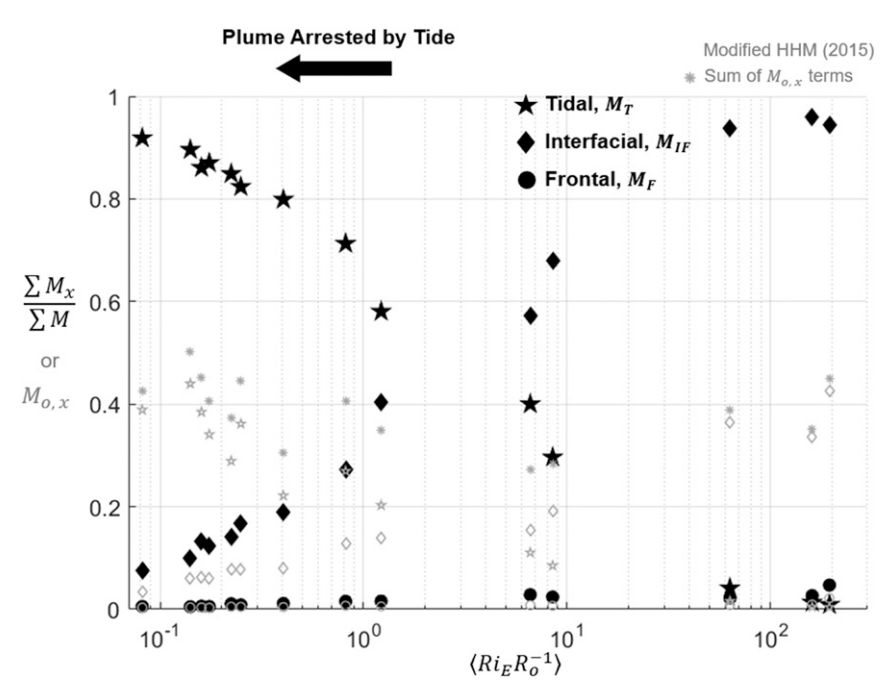


FIG. 10. Ratio of each tidally summed mixing power term to summed total input power, $\sum M_x / \sum M$, with x changing with the following terms: tidal mixing power M_T is denoted by stars, interfacial mixing power $M_{\rm IF}$ by diamonds, and frontal mixing power M_F by circles. Vertical axis is the dimensionless ratio, and horizontal axis is the tidally averaged dimensionless estuary Richardson number multiplied by the inverse Rossby number $\langle {\rm Ri}_E R_o^{-1} \rangle$ on a \log_{10} scale. An icon in $\langle {\rm Ri}_E R_o^{-1} \rangle < 1$ denotes a plume generally arrested by the tide. Icons in gray are estimates of each $M_{o,x}$ from the modified HHM15 method, with the sum of each $M_{o,x}$ term denoted with a gray asterisk.

Conversely, the discharge-dominated plumes (large $\langle Ri_E R_0^{-1} \rangle$) resulted in more interfacial mixing because of stronger stratification and shear in the plume layer which was not greatly influenced by tides (similar to Fig. 4a). Since plume spreading is a driving mechanism which allows for enhanced interfacial mixing (Hetland 2005), we propose that plume spreading is significantly halted as $\langle Ri_E R_0^{-1} \rangle$ decreases below unity. The alongshore tides created in these simulations effectively disrupt the spreadinginterfacial mixing balance for larger tidal amplitudes, as the tidal barotropic pressure gradient likely overtakes those at the river mouth and turns the plume downcoast. Spreading is further inhibited as shear from tidal processes contributes excess mixing to the plume and the alongshore tidal currents dominate plume transport relative to much smaller across shore currents (Fig. 3). This tidal influence on near-field evolution is visually evidenced by the tidally advected, asymmetric bulge shape shown in Fig. 3 that clearly diverges in along and cross-shore scales from the classically nontidal, radially spreading bulge from literature (Hetland 2005). Intratidal variability shown in Figs. 8 and 9 reveals that all $M_{\rm IF}$ curves peak prior to max ebb then minimize at max ebb when spreading is arrested. As spreading is reduced, shear at the plume interface and the associated mixing is minimized, and other mechanisms (tidal) become relatively more influential.

b. Tidal versus interfacial mixing: Spatial scales

Bottom-generated mixing is not typically considered an efficient mixing mechanism on pycnoclines in strongly stratified

systems (Holleman et al. 2016) which calls that mechanism into question. To investigate further, vertical sections of B, τ , shear production, $P = -\overline{u'w'}(\partial u/\partial z) - \overline{v'w'}(\partial v/\partial z)$ (where $\overline{u'w'}$ and $\overline{v'w'}$ are the Reynold's stresses in the x and y directions, respectively), and ϕ during a large tidal mixing experiment (Q = $1000 \,\mathrm{m}^3 \,\mathrm{s}^{-1}$, $\eta_{\mathrm{tide}} = 1.5 \,\mathrm{m}$) are shown at two interior plume locations to identify how interfacial and tidal mixing contributions change with increasing tidal currents (Fig. 11). The plume depth marked by dye (dashed line, Fig. 11a) can be related to the local minimum in shear stress (dotted line, Fig. 11b) to elucidate when interfacial mixing dominates relative to tidal. At a centralized plume coordinate just beyond the near field (x = 5 km, y = 0 km, left panels in)Fig. 11) d_{τ} , and therefore interfacial mixing, exists only prior to max ebb when P and τ are small near-bottom $(P \sim 10^{-7} \,\mathrm{m^2 \, s^{-3}} \text{ and } \tau \sim 10^{-5} \,\mathrm{m^2 \, s^{-2}}, \text{ hours 5-6, Figs. 11b,c)}.$ Simultaneously, a relatively stratified plume layer exists in the top few meters of the water column ($\phi = 100 \,\mathrm{J}$, Fig. 11d). Parameter d_{τ} generally is at the same depth as d_p at that time, implying that interfacial mixing controls plume dilution during slack water with negligible tidal mixing. As the tide progresses, P and τ increase near bottom (P ~ 10^{-4} m² s⁻³ and $\tau \sim 10^{-3} \,\mathrm{m}^2 \,\mathrm{s}^{-2}$, Figs. 11b,c) and expand upward to the surface (hours 6–7.5). Concurrently, d_{τ} disappears, the plume thickness expands to near the bottom, and the stratified plumeambient interface mixes into a more uniform, intermediate density class ($\sigma_{\theta} \sim 20$ –22 kg m⁻³, Fig. 11c) which extends to

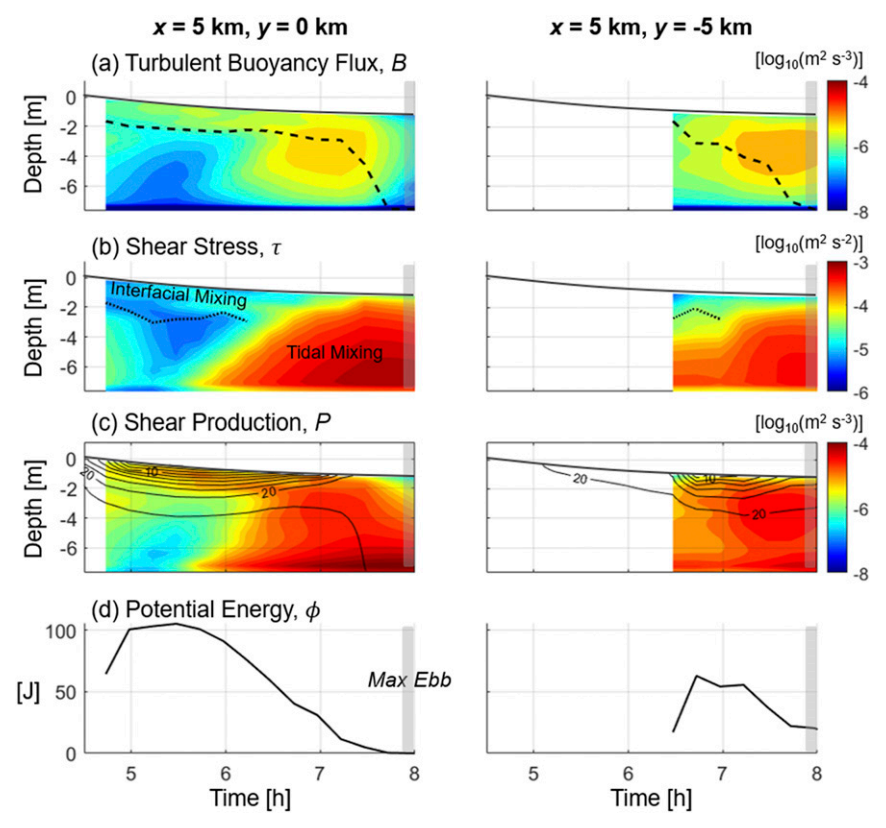


FIG. 11. Filled contours of (a) vertical turbulent buoyancy flux and plume depth (dashed line), (b) shear stress and shear stress local minimum (dotted line), (c) shear production, and (d) line plot of water column potential energy at (left) x=5 km, y=0 km and (right) x=5 km, y=-5 km near low water when Q=1000 m³ s⁻¹ and $\eta_{\rm tide}=1.5$ m. The y axis is depth, in meters, and x axis is time, in hours, for each subplot. All color bars are on a \log_{10} scale. Max ebb is marked with a gray box and the free surface with a black line. Contours of density anomaly, σ_{θ} , in 2 kg m⁻³ intervals are shown as solid black lines in (c) with 10 and 20 kg m⁻³ labeled.

near bottom and becomes much less stratified ($\phi = \sim 25 \, \mathrm{J}$, Fig. 11d). Buoyancy flux is maximized for the tidal cycle at this time (hours 6 to 7.5), and interfacial mixing does not exist, implying plume mixing transitions to a strong tidally mixed regime relative to the time of slack tidal currents. As the tide approaches max ebb, the water column is vertically homogenized and the plume fully mixed with the ambient ($\phi \sim 0 \, \mathrm{J}$ at hour 8, Fig. 11d).

At a separate, downcoast location ($x = 5 \,\mathrm{km}$, $y = -5 \,\mathrm{km}$, right panels in Fig. 11), the same general patterns occur after a later plume arrival time (\sim hour 6.5 when contours begin). Tidal mixing dominates (Figs. 11b,c) and the plume thickness expands to near bottom (Fig. 11a), but the plume layer remains stratified enough to not mix away completely (minimum $\phi \sim 25 \,\mathrm{J}$, Fig. 11d). An asymmetry in ϕ is therefore created, with the upcoast edge of the plume well mixed and weaker mixing on the downcoast side. We suspect the upcoast side of the plume is more susceptible to tidal mixing because the ambient waters approaching from that direction lack stratification, as demonstrated by larger salinity values upcoast of the plume during max ebb (\sim 32 g kg $^{-1}$) in Fig. 3. The heterogeneity in shelf stratification allows the mixed water beneath the plume to flow

away and be replaced with the near-ambient waters from outside the plume and quickly decrease ϕ . Downcoast, this effect is less defined as the mixed plume water class accumulates beneath that section of the plume, always allowing stratification to exist.

A decomposition of plume depth relative to total water depth in the horizontal extent (Fig. 12) corroborates the spatial patterns identified in Fig. 11. Contours of $d_p/(H + \eta)$ can be interpreted as the portion of the water column the plume comprises, with 1 indicating a plume mixed to the bottom. $d_p/(H+\eta)$ and ϕ for a relatively strong tidally mixed plume (Figs. 12a-c) are compared to a weaker tidal mixing experiment (Figs. 12d-f) during ebb. All regions of active interfacial mixing were flagged (anywhere d_{τ} is present, not shown), as were regions of active tidal mixing (no d_{τ} exists, not shown). For the significant tidal mixing scenario, a large portion of the plume footprint mixes to the bottom during maximum ebb currents at hour 8 and is biased to the upcoast side (Figs. 12a-c). For the moderate tide, only a small region (<3 km) beyond the estuary mouth mixes to the bottom (Figs. 12d-f). Relatively large ϕ (>70 J) and the existence of d_{τ} (not shown) near the mouth for all snapshots indicates a larger, bottom reaching

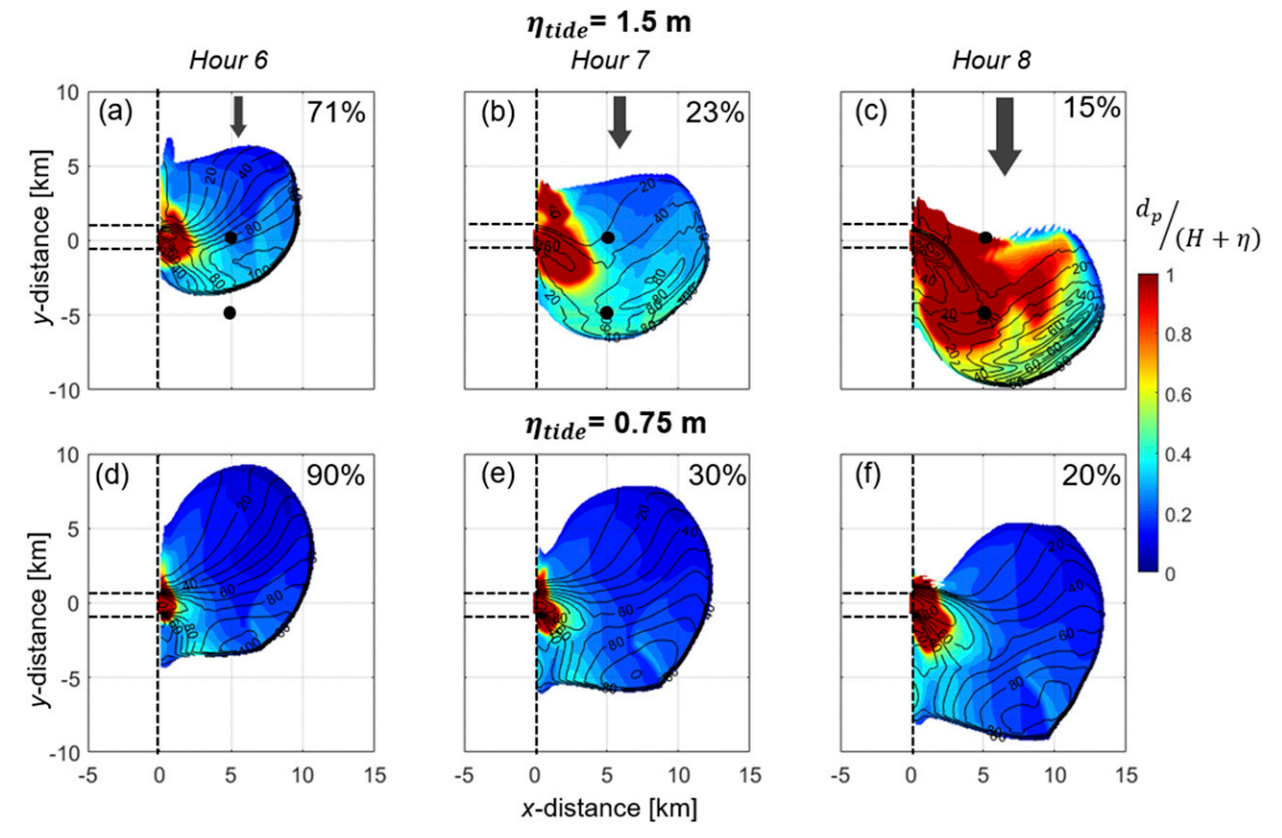


Fig. 12. Filled contours of plume depth d_p normalized by total water depth $(H + \eta)$ and labeled contours of ϕ (J) for $Q = 1000 \,\mathrm{m}^3 \,\mathrm{s}^{-1}$, (top) $\eta_{\mathrm{tide}} = 1.5 \,\mathrm{m}$ and (bottom) $\eta_{\mathrm{tide}} = 0.75 \,\mathrm{m}$ experiments. Snapshots show (a),(d) hour 6; (b),(e) hour 7; and (c),(f) hour 8 as ebb tidal currents increase. The spatial percentage of active interfacial mixing, based on d_τ (not shown), is denoted for each plot. Vertical axes are y distance (km), and horizontal axes are x distance (km). Current direction is denoted by the dark gray arrows, and general magnitude with arrow size. Black dots represent the locations of the time series from Fig. 10.

mixed layer exists beneath a still relatively fresh, surface plume layer (Fig. 4c) which is mixed through interfacial and tidal mechanisms. Beyond the mouth and near field, the regions which deepen or mix to the bottom exhibit smaller ϕ (0–20 J) and mixing is mostly tidal (no d_{τ}) or frontal (Fig. 12c). Further, interfacial mixing dominates spatially around slack water (71%–90% of the area, Figs. 12a,d) but tidal mixing takes over spatial dominance only as currents increase (70%–85% of area, Figs. 12b,c,e,f). Plumes feature a larger spatial extent of tidal mixing for a larger tidal amplitude relative to smaller amplitudes (larger percent tidal mixing in Figs. 12a-c than Figs. 12d-f). In all cases, tidal mixing never completely takes over in the near field, where discharge momentum likely allows spreading and interfacial mixing to continue, and near the leading front, where stratification maintains ($\phi > 80 \,\mathrm{J}$ in all snapshots). Stratification is always greatest at the leading, downcoast plume front ($\phi = 80\text{--}100 \,\text{J}$) and is weakest on the following, upcoast front ($\phi = 0$ –20 J), reinforcing the patterns identified in Fig. 11.

The asymmetric distribution of stratification and position of the plume observed in these experiments are likely also a result of straining and advection of the freshwater discharge and are briefly mentioned here. Straining can enhance or reduce vertical stratification through velocity shears deforming a water parcel, while advection moves the stratified water column via a depth averaged current. Former research on the Rhine river plume (also strongly tidally modulated) considers alongshore straining and advection to be important drivers of the time evolution of ϕ in the near and midfield plume (de Boer et al. 2008). Drawing loose comparisons to this work, it is likely that tidal straining is enhanced on both upcoast and downcoast sides of the plume footprint (excluding nearfield and seaward of it) because of significant horizontal density gradients and vertical shear (de Boer et al. 2008). Advection driven by tidal currents then pushes that strained water column into the interior or downcoast side of the plume, moving the plume and simultaneously enhancing stratification downcoast (Fig. 12). We suspect straining and advection driven increases in stratification is why tidal mixing cannot quite dominate the water column downcoast of the mouth.

c. On the effect of ambient stratification

Figures 11 and 12 shows plumes generally controlled by tidal mixing which can correspond to a sharp decrease in stratification in the water column. It is apparent that the intermediate density class associated with "old" plume water ($20 < \sigma_{\theta} < 22 \,\mathrm{kg}\,\mathrm{m}^{-3}$ beneath d_p in Fig. 11c) plays a part in enhancing the

buoyancy flux subplume (~4 m deep, Fig. 11a) as bottom stresses increase. Near-surface plume water mixes to that buoyancy after the plume interface deteriorates. Ultimately, although buoyancy flux from old plume stratification likely aided in the decay of the plume interface by weakening stratification between the layers, it was deemed insignificant in contributing excess mixing to M_T within the plume itself (appendix B). Although the simple evaluation provided in appendix B suggests the effect of ambient stratification is small on a strongly stratified tidal plume, the net influences from old plumes or coastal currents could be notable in some systems, and undoubtedly modifies mixing in some way. It is likely those effects would present themselves more clearly in plumes which originate nearer in salinity to the ambient shelf, or plumes analyzed at longer time scales than a single tide. Investigating the influence of ambient stratification on plume mixing mechanisms is a worthy topic to investigate in the future. However, for the tidal plumes presented here, we attribute bottom-generated shear production coupled with tidal currents arresting plume spreading as the main destructive mechanisms reducing near-surface shear at the plume interface and homogenizing shear throughout the water column (hours 6-6.5, Fig. 11b). Bottom-generated shear instabilities then mix the plume stratification and destroy the plume interface, evident in the patterns of P and ϕ discussed, which subsequently kills interfacial mixing, connects the plume to the bottom boundary layer, and mixes the plume, sometimes completely away on the sides exposed to strictly ambient currents (upcoast in these simulations). For the relatively weaker tide experiments, interfacial mixing covers a larger spatial extent of the plume and bottom-generated P and ε are weaker and less efficient at mixing near-surface plume waters (not shown).

6. Discussion

a. Comparison to theory

A theoretical ratio was developed in HHM15 to more accurately depict the mixing budget framework of Pritchard and Huntley (2006) and is similar to the ratio we present in Fig. 10. The HHM15 ratio, $M_o = 2(BA/g_f'Q)\gamma T^*$, approximates the rate of energy converted to mixing due to a specific process relative to the total energy required to mix the freshwater discharge from an initial density to a mixed ambient condition (differing from the total plume mixing over a tidal pulse we compare to in Fig. 10). In that estimate, A is the horizontal area over which a buoyancy flux B acts, T^* is the nondimensional fraction of time mixing occurs over, Q is discharge, and $\gamma = g_M'(g_f' - g_M')^{-1}$ with g_f' being the initial freshwater reduced gravity and g_M' is a final mixed reduced gravity. We modified the HHM15 mixing ratio to apply to model output by taking a time and volume integral of B, and tested it on these data as

$$M_{o,x} = \frac{2\iint BdV \, dt}{g_f' Qht} \gamma,\tag{10}$$

where x denotes the mixing process being analyzed (F = frontal, IF = interfacial, and T = tidal), h is the spatiotemporal average of plume depth, and t is the time period being analyzed

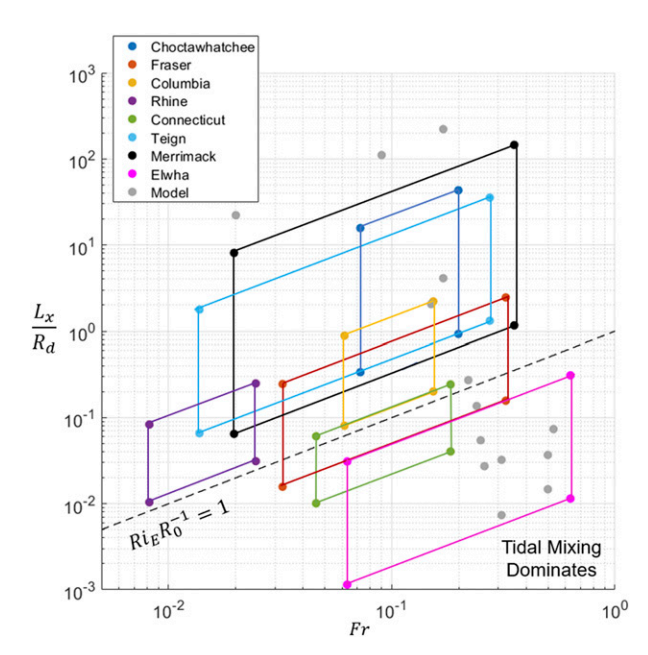


FIG. 13. Conceptual diagram showing the possible importance of tidal mixing on other river plume systems. Systems are plotted based on the ratio of plume-to-cross-flow length scale to the Rossby radius of deformation (vertical axis on a \log_{10} scale) and mouth Froude number range (horizontal axis on a \log_{10} scale). Each box represents a possible range of values based on spring to neap tidal variation and average to high river discharge cases. The parameter space of this work is plotted as the individual gray dots. Based on the results of this work, tidal mixing energy is prone to dominate the mixing energy budget when near or below the dotted 1:1 line shown ($Ri_E R_0^{-1} = 1$).

(12h in these runs). Estimates of $M_{o,x}$ are compared to $\sum M_x / \sum M$ in Fig. 10.

The relative importance of each mixing mechanism according to Eq. (10) is generally just under half of $\sum M_x/\sum M$ estimates with the same general trends holding (Fig. 10). For small $\langle \mathrm{Ri}_E R_o^{-1} \rangle$, tidal mixing $(M_{o,T})$ dominates and causes roughly 40% of plume mixing over a tidal cycle. For the largest $\langle \mathrm{Ri}_E R_o^{-1} \rangle$, tidal mixing is near zero and $M_{o,\mathrm{IF}}$ dominates with estimates at roughly 40%. The net sums of $M_{o,\mathrm{IF}}$, $M_{o,\mathrm{F}}$, and $M_{o,\mathrm{IF}}$ vary from 0.3 to 0.5, and imply that each plume created in these experiments does not completely mix out over one 12-h tide but rather is mixed about halfway to ambient conditions. This suggests the remaining 50%–70% of plume mixing occurs in the far-field plume at time scales beyond one tide. The estimates based on HHM15 provide context for the results of this work which give us a better understanding of the importance of plume mixing mechanisms on multiple time scales.

b. Applicability to other, tidally pulsed plumes

In many plume systems, the contribution to mixing from tidally generated bottom friction has been unknown or assumed negligible relative to interfacial and frontal processes. To put other shelf-plume systems in the context of this work, in Fig. 13 we normalize L_x and R_I by the deformation radius $R_d = \sqrt{g'h/f}$, presenting the mouth Froude

number, $R_I/R_d = U/\sqrt{g'h} = {\rm Fr}$, to characterize plumes. The Froude number, which relates plume input buoyancy to inertia, tends to increase with relatively higher discharge surface advected plumes that emerge from more time dependent salt wedge-like estuaries (Yankovsky and Chapman 1997). Note that $R_I \sim R_d$ is a critical plume, e.g., ${\rm Fr} \sim 1$, and therefore the metric L_x/R_d can be interpreted similarly to ${\rm Ri}_E R_0^{-1}$ as a comparison of the plume to cross-flow length scale to plume cross-shore length scale. Figure 13 illustrates when tidal mixing may be more important than interfacial mixing (i.e., tidal mixing mixes away most input buoyancy below the ${\rm Ri}_E R_0^{-1} = 1$ line). Since ${\rm Fr}$ was approximated for each system with discharge and mouth geometry from literature, both axes contain discharge as input and so all approximation boxes in Fig. 13 slope similarly to the ${\rm Ri}_E R_0^{-1} = 1$ line.

The $\langle Ri_E R_0^{-1} \rangle$ estimates are calculated using typical dry to wet season river discharges and spring to neap tidal ranges. Estimates are shown for the Fraser River plume (Halverson and Pawlowicz 2008; Kastner et al. 2018), the Columbia River plume (Akan et al. 2018; Spahn et al. 2009), the Rhine region of freshwater influence (ROFI) (Flores et al. 2017), the Choctawhatchee Bay plume (Huguenard et al. 2016), the Connecticut River plume (Whitney et al. 2016; Holleman et al. 2016), the Merrimack River plume (Hetland and MacDonald 2008), the River Teign plume (Pritchard and Huntley 2006), and the Elwha River plume (Warrick and Stevens 2011). The Connecticut and Elwha plumes, both of which exhibit shallow discharges and intense tidal modulation, are likely often dominated by tidal mixing. In the Columbia, Rhine, and Fraser River plumes, which all have variable discharges throughout the year, tidal mixing is likely important during some periods. In the Merrimack, River Teign, and Choctawhatchee Bay plumes, tidal currents are relatively weak over the shelf and tidal mixing is likely not important ever. Tides along more realistic, variable bathymetry of the plume systems listed will force a current ellipse different than what we see in these experiments with simple bathymetry and may have a different effect on the tidal mixing term in the energy budget. Further, differences in shelf slope beneath each plume would likely create spatial differences in tidal mixing, which are not captured by the depth and spatial average of tidal currents utilized in calculating the nondimensional numbers of Fig. 13. Plumes over steep shelf slopes may experience weakened tidal mixing due to a diminishing bottom boundary layer relative to total water depth. Results from the relatively gradual slope utilized in these simulations suggest tidal currents are slightly more effective at mixing plumes deeper into the water column nearer to shore in the shallow regions (Fig. 12). Nonetheless, these results provide a general framework which shows when tidal mixing could be more important than interfacial and frontal mechanisms.

c. Frontal mixing

Another noteworthy result of this work is the relative weakness of frontal mixing to interfacial and tidal processes in all experiments. The contribution of frontal mixing to a mixing budget has been highly uncertain. Estimates range from 100% (Pritchard and Huntley 2006) to 60% (Huguenard et al. 2016) to 20% (Orton and Jay 2005) and even less (Cole et al. 2020).

The results of this work are most nearly consistent with that of Cole et al. (2020), as frontal mixing never surpasses 10% of the total budget.

Frontal mixing is the mechanism least sensitive to changes in tide and discharge (Fig. 10), emphasizing that it never becomes important to the budget. Mixing magnitudes in the modeled front were often comparable to elsewhere in the plume (see Fig. 6b) meaning frontal mixing is likely sensitive to the plume area defined as the frontal zone, for which a definition will be more thoroughly addressed in future work. That area was small in all the experiments presented here relative to the remainder of the plume, even with the multiple liberal calculations of the frontal zone width which we employed. It is likely that smaller spatial scale plumes would exhibit a more important frontal mixing term within the budget, more in line with results from Pritchard and Huntley (2006). That said, frontal mixing may include significant convective instabilities which are not captured in this hydrostatic study. Applying a similar study to a nonhydrostatic model would offer more clarity and is an important topic for future research. Although determined from a hydrostatic model, these results still provide robust, synoptic estimates relative to the existing observed and heavily extrapolated point estimates reported in literature.

7. Conclusions

Tidal mixing has the potential to dominate the mixing budget of tidally pulsed meso/macrotidal river plumes for relatively large tides. Tidal mixing powers are between 50% and 90% of the total mixing for tidal amplitudes that successfully arrest plume spreading ($\langle Ri_E R_0^{-1} \rangle < 1$) whereas interfacial mixing is typically 10%-40% of mixing for those plumes. Interfacial mixing dominates the budget when spreading is not arrested by tides, accounting for 50%-95% of the budget. Frontal mixing never dominates the budget in this study, and never exceeds 10% of the total mixing energy. This is the first study to suggest that tidal mixing can exceed that of interfacial and frontal processes and is caused when bottom-generated shear production coupled with tidal currents arresting plume spreading reduce near-surface shear at the plume interface and homogenize shear throughout the water column. Tidal mixing within the plume may therefore be an important mechanism in determining total shelf mixing and circulation in meso/macrotidal regions influenced by surface advected plumes. The results of this work are thus important to consider for future modeling of riversourced pollutants and tracers into the ocean.

Acknowledgments. This project was funded by National Science Foundation Award 1756690. The authors thank Rob Hetland for useful suggestions on the methods, and the Advanced Computing Group at the University of Maine, which provided access to high-performance computing machines on which these experiments were performed. The authors also thank the two anonymous reviewers whose comments improved the original manuscript.

Data availability statement. Model output is available on request from Preston Spicer (preston.spicer@maine.edu).

APPENDIX A

Calculation Conditions

a. Interior grid points (k-points)

Condition 1: $d_{\tau} > d_p$ (interfacial mixing only, Fig. 4a)

$$M_{\rm IF} = \rho_0 \sum_{i=0}^{k} A_i \int_{d_{-}}^{\eta} B_i \, dz,$$
 (A1)

$$M_T = 0. (A2)$$

Condition 2: $d_{\tau} > d_{p}$ (interfacial and tidal mixing, Fig. 4c)

$$M_{\rm IF} = \rho_0 \sum_{i=0}^{k} A_i \int_{d_{\tau_i}}^{\eta} B_i \, dz \,, \tag{A3}$$

$$M_{T} = \left(\rho_{0} \sum_{i=0}^{k} A_{i} \int_{d_{\rho_{i}}}^{\eta} B_{i} dz\right) - \left(\rho_{0} \sum_{i=0}^{k} A_{i} \int_{d_{\tau_{i}}}^{\eta} B_{i} dz \rho_{0}\right). \quad (A4)$$

Condition 3: d_{τ} does not exist (tidal mixing only, Fig. 4b)

$$M_{\rm IF} = 0, \tag{A5}$$

$$M_T = \rho_0 \sum_{i=0}^k A_i \int_{d_{p_i}}^{\eta} B_i \, dz \,. \tag{A6}$$

b. Frontal grid points (j-points)

Condition 1: $d_{\tau} > d_f$ (frontal mixing only)

$$M_{\rm FR} = \rho_0 \sum_{i=0}^{j} A_i \int_{d_x}^{\eta} B_i \, dz,$$
 (A7)

$$M_T = 0. (A8)$$

Condition 2: $d_{\tau} > d_f$ (frontal and tidal mixing)

$$M_{\rm FR} = \rho_0 \sum_{i=0}^{j} A_i \int_{d_z}^{\eta} B_i \, dz \,, \tag{A9}$$

$$M_{T} = \left(\rho_{0} \sum_{i=0}^{j} A_{i} \int_{d_{f_{i}}}^{\eta} B_{i} dz\right) - \left(\rho_{0} \sum_{i=0}^{j} A_{i} \int_{d_{\tau_{i}}}^{\eta} B_{i} dz\right).$$
 (A10)

Condition 3: d_{τ} does not exist (tidal mixing only)

$$M_{\rm FR} = 0, \tag{A11}$$

$$M_T = \rho_0 \sum_{i=0}^{j} A_i \int_{d_{f_i}}^{\eta} B_i \, dz \,. \tag{A12}$$

APPENDIX B

Ambient Stratification

An empirical orthogonal function (EOF) analysis was performed for a large tide run which related tidal mixing power within the plume layer [Eq. (8)] to tidal mixing power in the

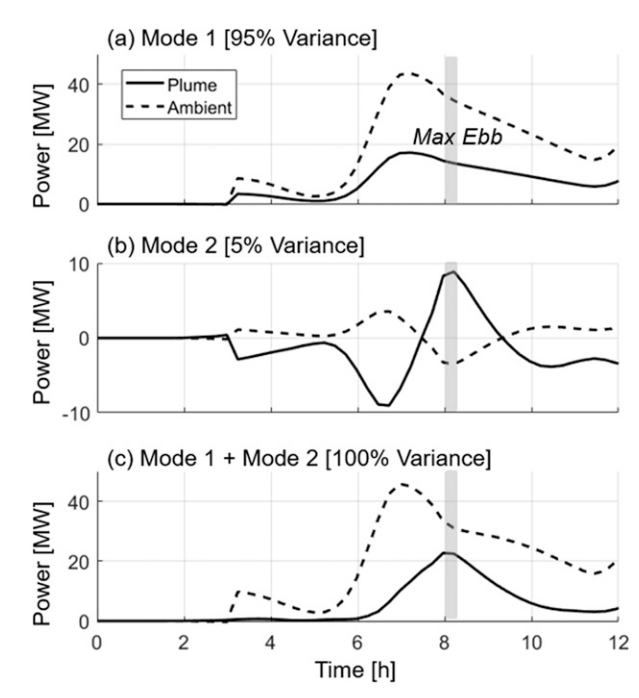


FIG. B1. EOF analysis modes of tidal mixing power (M_T) for the plume (solid, see Fig. 7d) and beneath-plume ambient (dashed) layers for $Q=1000~{\rm m}^3~{\rm s}^{-1}$ and $\eta_{\rm tide}=1.5~{\rm m}$. Modes (a) 1 and (b) 2 and (c) the sum of 1 and 2 are plotted. The x axis is time in hours, and the y axis is power in megawatts. Max ebb currents are marked with a gray box.

ambient layer beneath the plume: $M_A = \left[\rho_0 \sum_{i=0}^n A_i \int_{d_{p_i}}^H B_i dz \right]$, where H is the total depth of the water column. The modes in Fig. B1 are interpreted as

- Mode 1 is the tidal mode: the buoyancy flux and mixing power are completely from tidal mixing (comparable to Fig. 8d), which contributes a positive flux to both ambient and plume layers that maximizes near low water when currents are strongest.
- Mode 2 is the entrainment mode: it elucidates when buoyancy flux and mixing power is lost from one layer and given to the other. Mode 2 only accounts for 5% of the signal variance, implying buoyancy flux from ambient stratification beneath the plume does not significantly modify M_T as calculated here (i.e., by adding excess buoyancy to the plume).

APPENDIX C

Numerical Mixing

A moderate discharge and tide experiment ($Q = 500 \, \mathrm{m}^3 \, \mathrm{s}^{-1}$, $\eta_{\mathrm{tide}} = 0.75 \, \mathrm{m}$) was rerun and analyzed using the U3H horizontal advection scheme in ROMS (all other simulations in this work use MPDATA) (Fig. C1). The purpose of testing a different advection scheme was to identify the influence of numerical mixing on the energy budget approach utilized in this study. The U3H scheme causes the smallest amount of

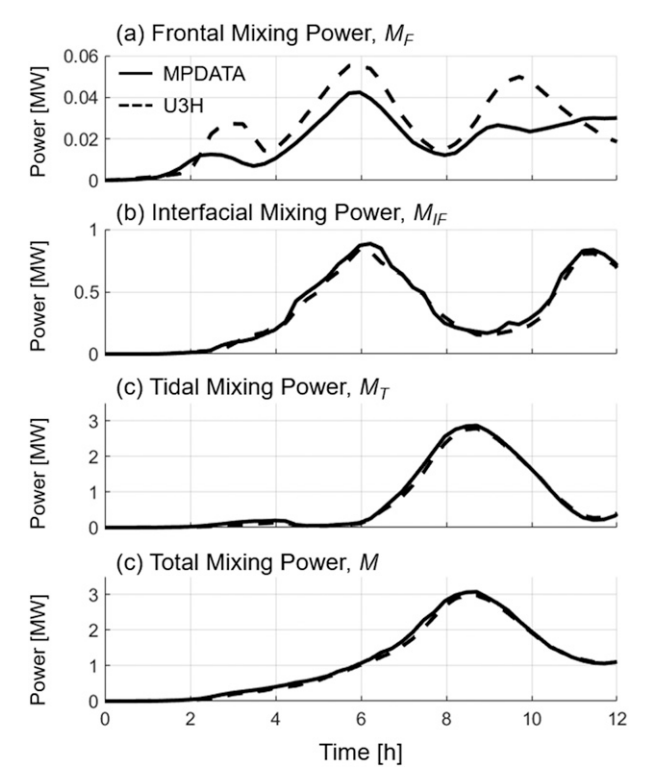


FIG. C1. Time varying instantaneous energy budget terms for the $Q=500\,\mathrm{m}^3\,\mathrm{s}^{-1},\,\eta_{\mathrm{tide}}=0.75\,\mathrm{m}$ experiment for two horizontal advection schemes. Panels show (a) frontal mixing power M_F , (b) interfacial mixing power M_{IF} , (c) tidal mixing power M_T , and (d) total plume mixing power M. Horizontal axes are time in hours. Solid lines denote the experiment run with MPDATA and dashed lines correspond to the experiment run with U3H.

numerical mixing relative to other commonly used schemes, which is why it was chosen to compare to here (Kalra et al. 2019). Numerical mixing is created by the discretization of the tracer transport advection term and can create spurious vertical mixing in 3D numerical models which would not exist in the real world. Numerical mixing can smear energy at salinity fronts which leads to a loss in the finer spatial structure at the front and a decrease in physical (real) mixing (Kalra et al. 2019). To accurately model and predict river plume mixing it is therefore important to estimate the importance of numerical mixing.

The most notable variation in mixing between advection schemes is in the frontal mixing term M_F , with variation up to 0.03 MW existing between the MPDATA and U3H runs (Fig. C1a). Differences between interfacial, tidal, and total mixing powers are less noted because of larger scaled y axes, but are likely of similar magnitude (Figs. C1b-d). MPDATA tends to underestimate frontal mixing but slightly overestimate the other terms.

The U3H scheme has been found to produce larger physical mixing than MPDATA (Kalra et al. 2019), indicating the larger M_F relative to MPDATA is not a product of increased numerical mixing, but rather from an increased physical mixing that is not saturated by numerical mixing. If

our calculations of frontal mixing (with MPDATA) were larger than the U3H values, this would indicate an estimate oversaturated with numerical mixing. These results fall in line with those of Kalra et al. (2019), as they found idealized, structured-grid experiments with strong external forcing produce the smallest relative contributions of numerical mixing. In general, this check between advection schemes indicates MPDATA is performing in a satisfactory manner, and ultimately changing schemes has a negligible effect on total plume mixing or the relative importance of each term to total mixing (Fig. C1).

REFERENCES

Akan, Ç., J. C. McWilliams, S. Moghimi, and H. T. Özkan-Haller, 2018: Frontal dynamics at the edge of the Columbia River plume. *Ocean Modell.*, 122, 1–12, https://doi.org/10.1016/ j.ocemod.2017.12.001.

Bowman, M. J., and W. E. Esaias, 1981: Fronts, stratification, and mixing in Long Island and Block Island sounds. *J. Geophys. Res.*, **86**, 4260–4264, https://doi.org/10.1029/JC086iC05p04260.

Burchard, H., and R. Hofmeister, 2008: A dynamic equation for the potential energy anomaly for analysing mixing and stratification in estuaries and coastal seas. *Estuarine Coastal Shelf Sci.*, **77**, 679–687, https://doi.org/10.1016/j.ecss.2007.10.025.

Canuto, V. M., A. Howard, Y. Cheng, and M. S. Dubovikov, 2001: Ocean turbulence. Part I: One-point closure model-momentum and heat vertical diffusivities. *J. Phys. Oceanogr.*, **31**, 1413–1426, https://doi.org/10.1175/1520-0485(2001)031<1413:OTPIOP> 2.0.CO;2.

Chapman, D. C., 1985: Numerical treatment of cross-shelf open boundaries in a barotropic coastal ocean model. J. Phys. Oceanogr., 15, 1060–1075, https://doi.org/10.1175/1520-0485(1985)015<1060:NTOCSO>2.0.CO;2.

Cole, K. L., and R. D. Hetland, 2016: The effects of rotation and river discharge on net mixing in small-mouth Kelvin number plumes. J. Phys. Oceanogr., 46, 1421–1436, https://doi.org/ 10.1175/JPO-D-13-0271.1.

—, D. G. MacDonald, G. Kakoulaki, and R. D. Hetland, 2020: River plume source-front connectivity. *Ocean Modell.*, **150**, 101571, https://doi.org/10.1016/j.ocemod.2020.101571.

de Boer, G. J., J. D. Pietrzak, and J. C. Winterwerp, 2006: On the vertical structure of the Rhine region of freshwater influence. *Ocean Dyn.*, 56, 198–216, https://doi.org/10.1007/s10236-005-0042-1.

—, —, and —, 2008: Using the potential energy anomaly equation to investigate tidal straining and advection of stratification in a region of freshwater influence. *Ocean Modell.*, 22, 1–11, https://doi.org/10.1016/j.ocemod.2007.12.003.

Fischer, H. B., 1972: Mass transport mechanisms in partially stratified estuaries. *J. Fluid Mech*, **53**, 671–687, https://doi.org/10.1017/S0022112072000412.

Fisher, N. R., J. H. Simpson, and M. J. Howarth, 2002: Turbulent dissipation in the Rhine ROFI forced by tidal flow and wind stress. *J. Sea Res.*, **48**, 249–258, https://doi.org/10.1016/S1385-1101(02)00194-6.

Flather, R. A., 1976: A tidal model of the north-west European continental shelf. *Mem. Soc. Roy. Sci. Liege*, 10 (6), 141–164.
Flores, R. P., S. Rijnsburger, A. R. Horner-Devine, A. J. Souza, and J. D. Pietrzak, 2017: The impact of storms and stratification on sediment transport in the Rhine region of freshwater influence. *J. Geophys. Res. Oceans*, 122, 4456–4477, https://doi.org/10.1002/2016JC012362.

- Garvine, R. W., 1974: Physical features of the Connecticut River outflow during high discharge. J. Geophys. Res., 79, 831–846, https://doi.org/10.1029/JC079I006P00831.
- —, 1977: Observations of the motion field of the Connecticut River plume. J. Geophys. Res, 82, 441–454, https://doi.org/ 10.1029/JC082i003p00441.
- —, and J. D. Monk, 1974:Frontal structure of a river plume.
 J. Geophys. Res., 79, 2251–2259, https://doi.org/10.1029/ JC079I015P02251.
- Geyer, W. R., and P. MacCready, 2014: The estuarine circulation. Annu. Rev. Fluid Mech., 46, 175–197, https://doi.org/10.1146/annurev-fluid-010313-141302.
- Haidvogel, D. B., and Coauthors, 2008: Ocean forecasting in terrainfollowing coordinates: Formulation and skill assessment of the Regional Ocean Modeling System. J. Comput. Phys., 227, 3595– 3624, https://doi.org/10.1016/j.jcp.2007.06.016.
- Halverson, M. J., and R. Pawlowicz, 2008: Estuarine forcing of a river plume by river flow and tides. J. Geophys. Res., 113, C09033, https://doi.org/10.1029/2008JC004844.
- Hetland, R. D., 2005: Relating river plume structure to vertical mixing. J. Phys. Oceanogr., 35, 1667–1688, https://doi.org/ 10.1175/JPO2774.1.
- —, and D. G. MacDonald, 2008: Spreading in the near-field Merrimack River plume. *Ocean Modell.*, 21, 12–21, https://doi.org/10.1016/j.ocemod.2007.11.001.
- Holleman, R. C., W. R. Geyer, and D. K. Ralston, 2016: Stratified turbulence and mixing efficiency in a salt wedge estuary. *J. Phys. Oceanogr.*, 46, 1769–1783, https://doi.org/10.1175/ JPO-D-15-0193.1.
- Horner-Devine, A. R., C. C. Chickadel, and D. G. MacDonald, 2013: Coherent structures and mixing at a river plume front. *Coherent Flow Structures at Earth's Surface*, Springer, 359–369.
- —, R. D. Hetland, and D. G. MacDonald, 2015: Mixing and transport in coastal river plumes. *Annu. Rev. Fluid Mech.*, 47, 569–594, https://doi.org/10.1146/annurev-fluid-010313-141408.
- Huguenard, K. D., and Coauthors, 2016: On the nature of the frontal zone of the Choctawhatchee Bay plume in the Gulf of Mexico. J. Geophys. Res. Oceans, 121, 1322–1345, https:// doi.org/10.1002/2015JC010988.
- Ivey, G. N., K. B. Winters, and J. R. Koseff, 2008: Density stratification, turbulence, but how much mixing? *Annu. Rev. Fluid Mech.*, 40, 169–184, https://doi.org/10.1146/annurev.fluid.39.050905.110314.
- Jia, Y., and M. M. Whitney, 2019: Summertime Connecticut River water pathways and wind impacts. J. Geophys. Res. Oceans, 124, 1897–1914, https://doi.org/10.1029/2018JC014486.
- Jones, G. R., J. D. Nash, R. L. Doneker, and G. H. Jirka, 2007: Buoyant surface discharges into water bodies. I: Flow classification and prediction methodology. *J. Hydraul. Eng.*, 133, 1010–1020, https://doi.org/10.1061/(ASCE)0733-9429(2007) 133:9(1010).
- Kakoulaki, G., 2015: Using Lagrangian surface drifters to study wind forcing and lateral spreading in a buoyant river plume. Ph.D. thesis, University of Massachusetts Dartmouth, 116 pp.
- ——, D. G. MacDonald, and K. Cole, 2020: Calculating lateral plume spreading with surface Lagrangian drifters. *Limnol. Oceanogr. Methods*, **18**, 346–361, https://doi.org/10.1002/ lom3.10356.
- Kalra, T. S., X. Li, J. C. Warner, W. R. Geyer, and H. Wu, 2019: Comparison of physical to numerical mixing with different tracer advection schemes in estuarine environments. *J. Mar. Sci. Eng.*, 7, 338, https://doi.org/10.3390/jmse7100338.
- Kastner, S. E., A. R. Horner-Devine, and J. Thomson, 2018: The influence of wind and waves on spreading and mixing in the

- Fraser River Plume. J. Geophys. Res. Oceans, **123**, 6818–6840, https://doi.org/10.1029/2018JC013765.
- Kilcher, L. F., J. D. Nash, and J. N. Moum, 2012: The role of turbulence stress divergence in decelerating a river plume. *J. Geophys. Res.* 117, C05032, https://doi.org/10.1029/2011JC007398.
- MacCready, P., N. S. Banas, B. M. Hickey, E. P. Dever, and Y. Liu, 2009: A model study of tide- and wind-induced mixing in the Columbia River Estuary and plume. *Cont. Shelf Res.*, **29**, 278–291, https://doi.org/10.1016/j.csr.2008.03.015.
- MacDonald, D. G., and W. R. Geyer, 2004: Turbulent energy production and entrainment at a highly stratified estuarine front. J. Geophys. Res., 109, C05004, https://doi.org/10.1029/ 2003JC002094.
- —, and A. R. Horner-Devine, 2008: Temporal and spatial variability of vertical salt flux in a highly stratified estuary. J. Geophys. Res., 113, C09022, https://doi.org/10.1029/2007JC004620.
- —, L. Goodman, and R. D. Hetland, 2007: Turbulent dissipation in a near-field river plume: A comparison of control volume and microstructure observations with a numerical model. *J. Geophys. Res.*, 3, C07026, https://doi.org/10.1029/2006JC004075.
- Marchesiello, P., J. C. McWilliams, and A. Shchepetkin, 2001: Open boundary conditions for long-term integration of regional oceanic models. *Ocean Modell.*, 3, 1–20, https://doi.org/10.1016/S1463-5003(00)00013-5.
- Nash, J. D., L. F. Kilcher, and J. N. Moum, 2009: Structure and composition of a strongly stratified, tidally pulsed river plume. J. Geophys. Res., 114, C00B12, https://doi.org/ 10.1029/2008JC005036.
- O'Donnell, J., 1997: Observations of near-surface currents and hydrography in the Connecticut River plume with the surface current and density array. *J. Geophys. Res.*, **102**, 25 021–25 033, https://doi.org/10.1029/97JC01008.
- —, S. G. Ackleson, and E. R. Levine, 2008: On the spatial scales of a river plume. J. Geophys. Res., 113, C04017, https://doi.org/ 10.1029/2007JC004440.
- —, and Coauthors, 2014: The physical oceanography of long Island Sound. Long Island Sound: Prospects for the Urban Sea, J. S. Latimer et al., Eds., Springer, 79–158.
- Orton, P. M., and D. A. Jay, 2005: Observations at the tidal plume front of a high-volume river outflow. *Geophys. Res. Lett.*, **32**, L11605, https://doi.org/10.1029/2005GL022372.
- Pritchard, M., and D. A. Huntley, 2006: A simplified energy and mixing budget for a small river plume discharge. *J. Geophys. Res.*, **111**, C03019, https://doi.org/10.1029/2005JC002984.
- Ralston, D. K., W. R. Geyer, J. A. Lerczak, and M. Scully, 2010: Turbulent mixing in a strongly forced salt wedge estuary. J. Geophys. Res., 115, C12024, https://doi.org/10.1029/ 2009JC006061.
- Rijnsburger, S., R. P. Flores, J. D. Pietrzak, A. R. Horner-Devine, and A. J. Souza, 2018: The influence of tide and wind on the propagation of fronts in a shallow river plume. *J. Geophys. Res. Oceans*, 123, 5426–5442, https://doi.org/10.1029/2017JC013422.
- Sherman, F. S., J. Imberger, and G. M. Corcos, 1978: Turbulence and mixing in stably stratified waters. *Annu. Rev. Fluid Mech.*, 10, 267–288, https://doi.org/10.1146/annurev.fl.10.010178.001411.
- Smolarkiewicz, P. K., and W. W. Grabowski, 1990: The multidimensional positive definite advection transport algorithm: Nonoscillatory option. *J. Comput. Phys.*, **86**, 355–375, https://doi.org/10.1016/0021-9991(90)90105-A.
- Spahn, E. Y., A. R. Horner-Devine, J. D. Nash, D. A. Jay, and L. Kilcher, 2009: Particle resuspension in the Columbia River

- plume near field. *J. Geophys. Res.*, **114**, C00B14, https://doi.org/10.1029/2008JC004986.
- Stacey, M. T., T. P. Rippeth, and J. D. Nash, 2011: Turbulence and stratification in estuaries and coastal seas. *Treatise on Estuarine and Coastal Science*, Vol. 2, Elsevier, 9–35, https://doi.org/10.1016/B978-0-12-374711-2.00204-7.
- Trenberth, K. E., L. Smith, T. Qian, A. Dai, and J. Fasullo, 2007: Estimates of the global water budget and its annual cycle using observational and model data. *J. Hydrometeor.*, **8**, 758–769, https://doi.org/10.1175/JHM600.1.
- Umlauf, L., and H. Burchard, 2003: A generic length-scale equation for geophysical turbulence models. J. Mar. Res., 61, 235–265, https://doi.org/10.1357/002224003322005087.
- Valle-Levinson, A., 2010: Contemporary Issues in Estuarine Physics. Cambridge University Press, 315 pp.
- Warrick, J. A., and A. W. Stevens, 2011: A buoyant plume adjacent to a headland—Observations of the Elwha River plume. Cont. Shelf Res., 31, 85–97, https://doi.org/10.1016/j.csr.2010.11.007.

- Whitney, M. M., D. S. Ullman, and D. L. Codiga, 2016: Subtidal exchange in eastern Long Island Sound. *J. Phys. Oceanogr.*, **46**, 2351–2371, https://doi.org/10.1175/JPO-D-15-0107.1.
- Winters, K. B., P. N. Lombard, J. J. Riley, and E. A. D'Asaro, 1995: Available potential energy and mixing in density-stratified fluids. J. Fluid Mech, 289, 115–128, https://doi.org/10.1017/ S002211209500125X.
- Wunsch, C., and R. Ferrari, 2004: Vertical mixing, energy, and the general circulation of the oceans. *Annu. Rev. Fluid Mech.*, 36, 281–314, https://doi.org/10.1146/annurev.fluid.36.050802.122121.
- Yankovsky, A. E., and D. C. Chapman, 1997: A simple theory for the fate of buoyant coastal discharges. *J. Phys. Oceanogr.*, 27, 1386–1401, https://doi.org/10.1175/1520-0485(1997)027<1386: ASTFTF>2.0.CO;2.
- Yuan, Y., and A. R. Horner-Devine, 2013: Laboratory investigation of the impact of lateral spreading on buoyancy flux in a river plume. *J. Phys. Oceanogr.*, 43, 2588–2610, https://doi.org/10.1175/JPO-D-12-0117.1.